CORE
Metadata, citation and similar papers at core.ac.uk
Provided by Utrecht University Repository

Dynamics of the Solar Chromosphere. II. Ca II H_{2V} and K_{2V} Grains versus Internetwork Fields

B. W. Lites
High Altitude Observatory, National Center for Atmospheric Research, P.O. Box 3000, Boulder CO 80307-3000

R. J. Rutten
Sterrekundig Instituut, Postbus 80 000, NL–3508 TA Utrecht, The Netherlands

T. E. Berger
Lockheed-Martin Solar and Astrophysics Lab, Dept. H1-12, Bldg. 252, 3251 Hanover St., Palo Alto, CA 94304

Abstract

We use the Advanced Stokes Polarimeter at the NSO/Sacramento Peak Vacuum Tower Telescope to search for spatio-temporal correlations between enhanced magnetic fields in the quiet solar internetwork photosphere and the occurrence of Ca II H_{2V} grains in the overlying chromosphere. We address the question of whether the shocks that produce the latter are caused by magnetism-related processes, or whether they are of purely hydrodynamic nature. The observations presented here are the first in which sensitive Stokes polarimetry is combined synchronously with high-resolution Ca II H spectrometry. We pay particular attention to the nature and significance of weak polarization signals from the internetwork domain, obtaining a robust estimate of our magnetographic noise level at an apparent flux density of only 3 Mx cm^{-2}. For the quiet Sun internetwork area analyzed here, we find no direct correlation between the presence of magnetic features with apparent flux density above this limit and the occurrence of H_{2V} brightenings. This result contradicts the one-to-one correspondence claimed by Sivaraman & Livingston (1982). We also find no correspondence between H_{2V} grains and the horizontal-field internetwork features discovered by Lites et al. (1996).

1 Introduction

This paper continues studies of dynamical phenomena in the solar chromosphere as displayed by the Ca II H & K resonance lines at $\lambda = 396.849$ nm and 393.368 nm. An earlier study (Lites, Rutten & Kalkofen 1993; henceforth Paper I) concentrated on the dynamics of chromospheric network elements. We now turn to the internetwork domain, i.e., the areas of quiet-Sun chromosphere that overlie photospheric supergranulation cell interiors and that are bordered by the irregularly patterned chromospheric network. In particular, we address the long-standing issue whether the so-called Ca II H_{2V} and K_{2V} grains, which intermittently appear within internetwork areas, mark sites of enhanced magnetic field. In order to clarify this issue, we begin by reviewing its context.

1.1 H_{2V} and K_{2V} Grains

The major dynamical phenomenon displayed by the Ca II H & K lines in internetwork regions consists of the "chromospheric three-minute" oscillation. This is neither a purely chromospheric nor a purely three-minute wave mode (e.g., Kulaczewski 1992); the term describes the wide-band ($f \approx 3 - 8$ mHz) modulation peak that gradually replaces the five-minute p-mode peak in temporal power spectra describing Doppler shift or intensity variations measured at increasing height of forma-

tion (Fig. 1 of Noyes 1967, reprinted as Fig. 1 of Rutten 1995). This modulation occurs in a "mesoscale" pattern in which the characteristic patches of coherent oscillation measure a few arcseconds, somewhat smaller than the coherent patches resulting from p-mode interference in the photosphere (Fig. 3 of Paper I). In movies constructed from high-resolution (i.e., of order 1 arcsec) Ca II K filtergrams the oscillation pattern is seen as wispy, thread-like texture displaying rapid morphology changes which often give the impression of highly supersonic proper motion over the surface. The H_{2V} and K_{2V} grains are intermittent, localized enhancements of this dynamical brightness pattern. They last less then a minute, often re-appear a few times at 2–4 min intervals at about the same place, and frequently occur in pairs. They are spectrally limited to a narrow wavelength band ($\Delta\lambda \approx 8$ pm) about 16 pm to the violet of the H & K line centers (e.g., Cram & Damé 1983; Figs. 1–2 of Paper I; Fig. 3 of Hofmann et al. 1996). This property is the defining one that gave K_{2V} grains their name, but their spatio-temporal pattern is part of the wider band line-center modulation (Fig. 2 of Rutten 1994, Fig. 1 of Rutten et al. 1999).

Figures 1–3 illustrate the K_{2V} grain pattern using images from high-quality Ca II K and G band (CH lines around $\lambda = 430.5$ nm) filtergram sequences taken by R.A. Shine with the Swedish Vacuum Solar Telescope at La Palma on October 5, 1995. They are part of a data set described and analyzed in more detail by Loefdahl et al. (1998) and Berger et al. (1998); the reduction included restoration of the G-band images with phase-diverse speckle techniques. The Ca II K filter had a $\Delta\lambda = 0.3$ nm passband containing the core of the Ca II K line at $\lambda = 393.3$ nm. The 70-min temporal average in the lower panel of Fig. 1 demonstrates the rapid variation of the internetwork brightness patterning by showing considerable suppression of its time-averaged contrast relative to the network, when compared with the individual snapshot in the upper panel.

Figure 2 illustrates that the network bright points ("patches") seen in Ca II K overlie clusters of smaller scale G-band bright points. The latter are unresolved even at 0.2 arcsec resolution, lie within intergranular lanes, and mark locations of strong-field flux elements (Berger 1997). The three isolated Ca II K features that are marked in the upper panel behave similarly to the "persistent flasher" of Brandt et al. (1992, 1994). The full image sequence shows that the identified features brighten at irregular intervals while migrating at subsonic speed. Each of the three Ca II K features is accompanied by intermittent G-band bright points in the underlying photosphere, as seen in the lower panel for this image pair. The G-band bright points travel along intergranular lanes at local flow speeds. They become distorted or fragment or combine in very dynamical fashion set by the evolution of the surrounding granules, but nevertheless maintain a long-term identity that signifies the

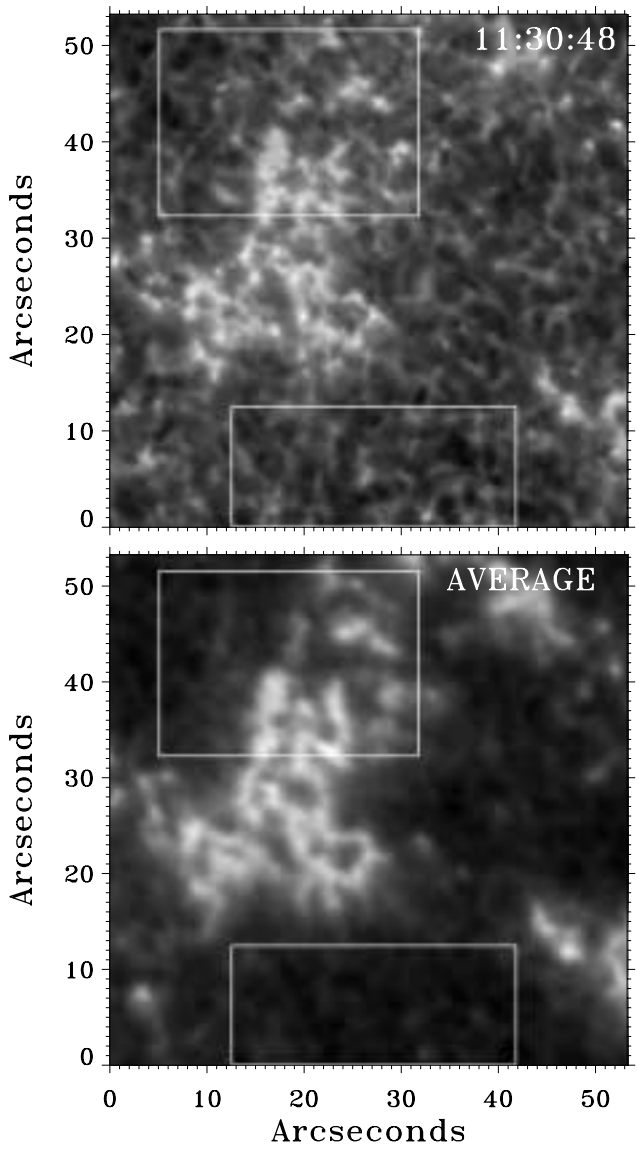

Figure 1: A high-resolution (sub-arcsec) Ca II K filtergram (upper panel) of the solar surface taken with the Swedish Vacuum Solar Telescope shows both active network (or small plage) which appears bright in Ca II K, and quiet internetwork which is considerably darker. The area outlined by the upper rectangle is compared to the underlying photosphere in Fig. 2. The lower rectangle outlines a quiet internetwork area shown also at subsequent moments in Fig. 3. The Ca II K emission pattern consists of elongated ridges with localized enhancements. The lower panel is a temporal average over the 70-min filtergram sequence. The network patches remain stably present and retain high contrast in the average. The internetwork pattern changes rapidly and therefore has greatly reduced contrast in the time average.

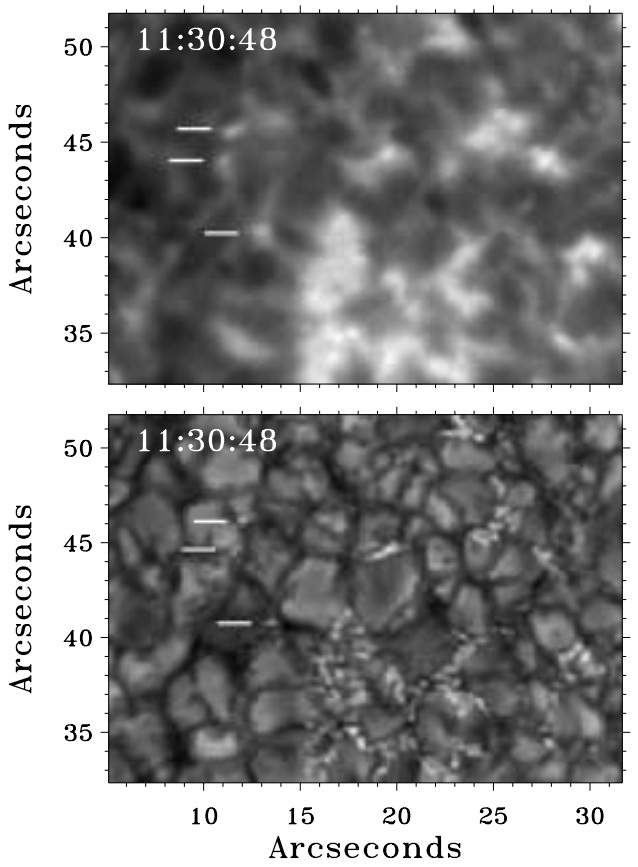

Figure 2: A comparison of a partial Ca II K filtergram, corresponding to the upper rectangle in Fig. 1, with a simultaneous G-band image demonstrates the magnetic origin of the bright Ca II K emission patches. The G band image maps the underlying photospheric granulation at 0.2 arcsec resolution (the telescope diffraction limit reached by phase-diverse speckle restoration) and shows tiny bright points that mark strong-field flux elements. The three isolated features that are marked in the upper panel might be taken to represent internetwork K_{2V} grains from this single Ca II K snapshot, but when the image sequences are displayed as movies they are seen to represent "persistent flashers" that correspond to intermittently present G-band bright points in the photosphere.

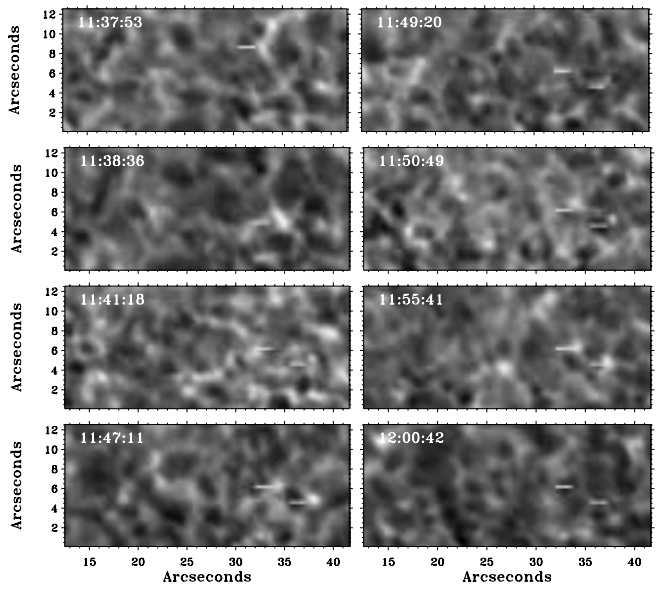

Figure 3: The wispy pattern of the internetwork domain and its rapid variation are illustrated by selected frames from the La Palma Ca II K sequence. The area corresponds to the lower rectangle in Fig. 1. The markers in the first two frames, taken only 43 sec apart, identify the apparent supersonic motion (70 km s^{-1}) of a brightening which travels along a pattern ridge. The two markers in the other panels (at fixed locations) identify two concurrent recurrent K_{2V} grains which brightened, in phase, a few times at 2–3 min intervals.

presence of magnetic field.

Finally, Fig. 3 shows examples of the wispy, rapidly changing texture which may be seen continuously nearly everywhere in the internetwork. The first two panels illustrate a case of supersonic apparent motion (cf. Steffens et al. 1996, Wellstein et al. 1998), while the other panels show repetitive appearance of a pair of adjacent K_{2V} grains. These filtergrams contain no information on the spectral signature of the emission features across the K-line core, so they do not reveal whether they are "regular" K_{2V} grains; i.e., whether their emission is limited to the K_{2V} peak alone. However, they are likely to be K_{2V} grains because the texture in these filtergrams is set largely by the inner-wing whiskers which precede the grains (cf. the spectral displays in Figs. 4–5 of Cram & Damé 1983 and Fig. 3 of Hofmann et al. 1996) but display the same spatio-temporal pattern (Rutten 1994, Rutten et al. 1999).

It is also not known whether the migrating "persistent flasher" of Brandt et al. (1992, 1994) and the three features marked in Fig. 2 emit primarily at K_{2V} or whether they represent a core-wide enhancement similar to that of network elements. There are no such flashers obviously present in the spectral data presented in this paper so that this question remains open. In any case, at locations well away from the network the flasher phenomenon is rare compared to the ubiquitous K_{2V} internetwork grain/whisker activity.

The extensive older literature on this subject is of both observational and interpretive nature and dates back to Hale & Ellerman (1904). It has been reviewed at length by Rutten & Uitenbroek (1991a) who concluded that most grains are of acoustic origin and mark sites of constructive interference between multiple wave modes. Rutten & Uitenbroek ended their review by predicting that the question why the grains appear should soon be

answered. By now that is indeed the case, but the questions of where the grains appear and whether their locations possess diagnostic value are yet open. We address these here.

The more recent literature on this topic has been reviewed by Rutten (1994, 1995, 1996). The most important development consists of the successful reproduction of repetitive K_{2V} and H_{2V} grain formation by Carlsson & Stein (1992, 1994, 1995, 1997) whose work crowns a sequence of earlier wave modeling efforts (e.g., Leibacher et al. 1982; Rammacher & Ulmschneider 1992; Fleck & Schmitz 1991b, 1993; Kalkofen et al. 1994; Sutmann & Ulmschneider 1995a, 1995b). Carlsson & Stein's one-dimensional radiation-hydrodynamics simulations of some of our data presented in Paper I have definitely confirmed that the repetitive grains mark acoustic shock interactions in which fast (order of 10 km s^{-1}) post-shock down flows interact with fresh shocks that result from the steepening of upward propagating acoustic waves. Carlsson & Stein have thus confirmed the earlier suggestions of Athay (1970), Cram (1972), and Liu & Skumanich (1974), the forward data inversion of Mein et al. (1987), and the grain-formation scenario of Rutten & Uitenbroek (1991a, 1991b). At two of the four solar locations simulated by Carlsson & Stein (1997) the correspondence between computed and observed Ca II H spectral behavior is excellent even in detail; for the two other locations the observations and computations are sufficiently similar to accept the latter as a qualitatively valid reproduction of the solar phenomenon. In addition, Carlsson & Stein (1997) show diagnostic diagrams and results from experiments which clarify to large extent *how* H_{2V} and K_{2V} grains form spectrally. The shocks themselves remain weak; they do not lift or heat the time-averaged chromosphere substantially. However, they nevertheless make the internetwork chromosphere a medium that is far too dynamic to be described by traditional hydrostatic modeling (Carlsson & Stein 1995).

The Carlsson-Stein simulations are one-dimensional and do not answer the question why grains occur *where* they do. The success of the simulations indicates that the internetwork chromosphere portrayed by Ca II H & K is largely controlled by the directly underlying photosphere, a fact that was earlier established observationally by measuring large coherence and well-defined phase relationships co-spatially between photospheric and chromospheric internetwork oscillations (e.g., Deubner & Fleck 1990; Paper I). However, it should be noted that the Carlsson-Stein simulation piston, located slightly below the surface in their model, was derived directly from our data by constraining it to reproduce the observed Doppler excursions of the photospheric Fe I 396.682 nm line shown in Fig. 3 of Paper I. The simulations therefore contained implicitly all non-local influences that affected the actual formation of Fe I 396.682 nm, such as the *p*-mode interference patterns, the granular dynamics and the mesoscale and supergranular flows. In particular, there was no magnetic field in the Carlsson-Stein simulations, but if solar magnetism influenced the Fe I 396.682 nm Doppler signal in some way, some of that influence might be accounted for through the inferred subsurface piston modulation.

A direct relation between K_{2V} grain occurrence and internetwork magnetism was claimed by Sivaraman & Livingston (1982; cf. Sivaraman 1991; Kariyappa et al. 1994) who blinked a one-hour sequence of Ca II K spectroheliograms against two Fe I 868.8 mm magnetograms taken just before and after, and found that *all* K_{2V} grains correspond one-to-one to magnetic internetwork features, with a qualitative correlation between grain brightness and magnetic field strength. Magnetic anchoring of the grains was also suggested by Damé and coworkers (Damé et al. 1984; Damé 1985; Damé & Martić 1987, 1988) on the basis of the apparent "location memory" implied by repetitive grain appearances in Ca II K filtergram movies.

The existence of one-to-one correspondence between K_{2V} grains and field enhancements has often been doubted. Rutten & Uitenbroek (1991a) suggested that it concerns only exceptional patches such as the flasher above but that the prevalent K_{2V} grain phenomenon is set primarily by non-magnetic wave interference. This suggestion has since been supported observationally by Kneer & Von Uexkull (1993), Von Uexkuell & Kneer (1995), Steffens et al. (1996), Hofmann et al. (1996), Remling et al. (1996), and Nindos & Zirin (1998). Appropriate non-magnetic pistons, if identifiable at all, might then consist of the peak amplitudes in the *p*-mode interference pattern (Steffens et al. 1996; Hofmann et al. 1996), convective downdrafts in intergranular lanes (Rutten 1995), or even faster subsurface downflow plumes (Hoekzema & Rutten 1998).

Theoretical work on the piston issue has so far been restricted to discussions of the amount of 3-min power present in the Carlsson-Stein piston by Cheng & Yi (1996) and Theurer et al. (1997). The latter authors suggest that atmospheric filtering produces the excess of 3–min power observed for the Fe I 396.682 nm line in Paper I as compared to the subsurface prediction from the Lighthill-Stein theory for turbulent convection (Lighthill 1952; Stein 1967; Musielak et al. 1994). They so imply that the subsurface pistons driving the K_{2V} grains result from convection in straightforward fashion. However, Kalkofen (1989, 1990, 1991, 1996) has also furnished speculations in which internetwork fields play a key role in various disguises, ranging from kiloGauss flux tubes down to weak fields. His latest suggestion invokes collisions between medium-strong (500 G or more) internetwork flux tubes and granules (Kalkofen 1996).

In summary, the issue of correspondence between internetwork K_{2V} grains and internetwork field elements is not conclusively resolved. A major source of the uncertainty arises from limitations of observational technique, which we confront directly with the observations reported herein. Internetwork fields present a similarly open issue, to which we turn now.

1.2 Internetwork Magnetism

Solar internetwork fields remain elusive entities (e.g., Zwaan 1987, and the excellent introductory review to Keller et al. 1994). The initial report by Livingston & Harvey (1971) described their appearance as ubiquitous bipolar patterns of random nature in which the single-polarity patches extend over 2–10 arcsec. Harvey (1977) specified a mixed-polarity pattern with element diameters of about 2 arcsec and net fluxes (area-integrated apparent field strength) of about 5×10^{16} Mx per element.

More recently, Keller et al. (1994) derived a sub-kiloGauss upper limit to the intrinsic field strength $|\vec{B}|$ of a few isolated high-signal internetwork field patches with size about 3 arcsec and total flux about 1×10^{17} Mx. An average value $|\vec{B}| \approx 500$ Gauss was reported by Lin (1995) for those internetwork features observed at 1.56 μm that were strong enough to exceed his sensitivity cutoff at flux density 1.5×10^{16} Mx per 0.48 arcsec^2 spatial sample, or $B_{\rm app}^{\rm BBSO} > 6$ Mx cm^{-2} where $B_{\rm app}^{\rm BBSO}$ stands for the apparent flux density measured in this particular data set at the Big Bear Solar Observatory (BBSO)[1]. Internetwork features with such field strength make up a relatively rare class, as evident from the BBSO quiet Sun magnetogram that is shown (rather confusingly at three different orientations) in Fig. 1 of Wang et al. (1995), Fig. 1 of Zirin (1995) and Fig. 1 of Lee et al. (1997), and which belongs to a sequence called the "best ever BBSO quiet-sun one" by Zhang et al. (1998) who also show parts of other frames (at yet another orientation). The internetwork fields in this map are not ubiquitously filling the cell interiors but stand out as isolated patches, "distinguished against field-free background" (Lee et al. 1997). Lin (1995) attributed them to ensembles of thin magnetostatic flux tubes. Solanki et al. (1996) supported this view and suggested that they are due to weak convective collapse. At a professed resolution of 2 arcsec the distributions of flux per observed patch are distinct from that of the strong-field network features (Wang et al. 1995), indicating intrinsically different nature (cf. Lee et al. 1997; Meunier et al. 1998). These internetwork patches tend to appear initially with mixed polarity, to migrate towards the supergranulation cell borders and to disappear quickly, often through merging or cancellation; they may be the most important source of magnetic flux to sustaining the quiet Sun network (Wang et al. 1996; Schrijver et al. 1997; Zhang et al. 1998).

The "salt-and-pepper" general background pattern reported by Livingston & Harvey (1971) and Harvey (1977) has not been discussed recently, but it is present in Fig. 4 of Lites et al. (1996) as rather grey, relatively noisy areas away from the "bloom" of network patches.

In addition to the ubiquitous background pattern and the stronger $B_{\rm long} \approx 500$ Gauss vertical-field features studied at BBSO, Lites et al. (1996) found horizontal internetwork fields (HIFs), apparent only in Stokes Q and U, that are characterized by predominantly horizontal flux orientation. They are short-lived (5 min), compact (sub-arcsecond), and intrinsically weak ($|\vec{B}|$ well below 1 kiloGauss).

Finally, truly weak background fields may exist as well. The Hanle depolarization estimates of Faurobert-Scholl (1993) and Bianda et al. (1998) indicate an upper limit well below $|\vec{B}| = 100$ Gauss. However, their existence in the low chromosphere has recently been brought into question by the application of detailed atomic and radiative transfer computations including the effects of lower-level polarization to observed polarization profiles of the Na I D-lines (Landi Degl' Innocenti 1998).

1.3 Internetwork Grains versus Internetwork Fields

Since Sivaraman & Livingston (1982) claimed a one-to-one relationship, only two papers, both recent, have addressed the issue of grain–field correspondence observationally. The first is by Remling et al. (1996) who adopted spectral brightening in the CN band head at $\lambda = 388.3$ nm as a proxy for the presence of strong-field flux tubes and compared CN spectrograms to simultaneous Ca II K spectrograms covering a 6×340 arcsec^2 area. They found that K_{2V} grain locations brighten simultaneously in CN, with 4-5 min modulation over 10 to 15 min duration, but without the longer-lasting CN enhancement expected for long-lived internetwork field elements as the ones recorded by Sivaraman & Livingston (1982). Remling et al. (1996) conclude that the CN enhancements portray the same upper-photospheric modulation that is evident in the inner-wing Ca II H & K "whiskers" (Beckers & Artzner 1974), and that the absence of longer-duration enhancement excludes one-to-one alignment between K_{2V} grains and strong-field flux tubes.

[1] Measured Stokes V/I circular polarization signals translate into apparent flux density estimates which only rarely equal actual solar field strengths $|\vec{B}|$, and which are strongly instrument- and seeing-dependent, a point to be emphasized at the outset and elaborated in Sect. 3 below. Following Sect. 2.1 of Keller et al. (1994), we distinguish the two quantities throughout this paper by expressing apparent flux density $B_{\rm app}$ in Mx cm^{-2} and intrinsic solar field strengths $|\vec{B}|$ and $B_{\rm long}$ (the longitudinal component of the field) in Gauss.

The other recent paper on grain-field correspondence is by Nindos & Zirin (1998) and is not limited to strong-field elements. It combines BBSO magnetograms with co-temporal Ca II K filter images and represents a much more direct repeat of the observations of Sivaraman & Livingston (1982). The images were not taken strictly simultaneously, but K filtergrams were selected that were taken within a few minutes of a magnetogram construction. Bright K features were then compared with magnetogram features. The first conclusion is that the K-line intensity increases linearly with the apparent flux density $B_{\rm app}^{\rm BBSO}$ for network elements with $B_{\rm app}^{\rm BBSO} > 10$ Mx cm^{-2}. In the internetwork domain which they defined to be $B_{\rm app}^{\rm BBSO} < 10$ Mx cm^{-2}, Nindos & Zirin (1998) find a dichotomy between two types of K-line brightenings: fairly scarce long-lived "magnetic brightenings" with apparent field strength above the average noise level, and more widespread weaker "non-magnetic brightenings" with apparent field strength below the noise level. The latter was estimated at a few Mx cm^{-2} as determined by subtracting successive magnetograms. The "magnetic" K brightenings were found to migrate at about 1 km s^{-1}, characteristic of the mesoscale convection flow speeds, whereas the "non-magnetic" K brightenings were found to live shorter and to move at much larger apparent speeds, of order 40 km s^{-1}. Although Nindos & Zirin (1998) did not use temporal modulation of the latter features as a diagnostic, it seems likely that these correspond to K_{2V} grain behavior as illustrated in Fig. 2, whereas their "magnetic brightenings" correspond to features as the ones that are marked in Fig. 2 and are akin to the internetwork flasher of Brandt et al. (1992, 1994). We think it likely that the "magnetic brightenings" correspond to the relatively strong internetwork field elements studied by Lin (1995), Wang et al. (1995), Wang et al. (1996), Lee et al. (1997), and Zhang et al. (1998).

In this paper we take a more quantitative approach to test the Sivaraman & Livingston (1982) conjecture by utilizing spectrographic techniques to enhance the measurement accuracy at the expense of field-of-view. First, we use high-resolution Ca II H spectrograms to define a H_{2V} grain wavelength band that is considerably narrower than the 0.11 nm spectroheliograph bandpass used by Sivaraman & Livingston (1982) which sampled the full Ca II K_{232} line core. Second, we observed an area which is truly quiet[2], in contrast to the partial Ca II K heliogram that is reproduced (at unspecified scale) in Sivaraman & Livingston (1982) and is very crowded with what seems active rather than quiet network in addition to plage. Third, we did not take magnetograms only before and after the spectral sequence, but have obtained Ca II H spectra and Fe I 630.3 nm Stokes diagnostics synchronously and continuously. Fourth, we used the NSO Vacuum Tower Telescope at Sacramento Peak at fairly good seeing, achieving angular resolution (1 – 2 arcsec) undoubtedly better than that of Sivaraman & Livingston (1982). Finally, we used the HAO/NSO Advanced Stokes Polarimeter (ASP) of which the reliability and sensitivity in full-vector magnetic field measurements has been established beyond doubt (e.g., Lites et al. 1994; Lites 1996; Skumanich et al. 1997). In general, ASP observations of the Zeeman-sensitive Fe I 630 nm lines together with the elaborate ASP calibration and analysis procedures provide exceptionally sensitive measures of active region, network and internetwork magnetic field characteristics. For example, the time series records by Lites et al. (1998) of sunspot umbrae in which the temporal variations in the inferred intrinsic field strengths $|\vec{B}|$ remain within only a few Gauss, the precision measurements of the vector fields of solar plage by Martínez Pillet et al. (1997), and the discovery of HIFs by Lites et al. (1996). have demonstrated the sensitivity of the ASP to both weak and strong fields in the solar photosphere. We show below that the ASP discerns internetwork fields down to $B_{\rm app}^{\rm ASP} \approx 3$ Mx cm^{-2} in the data analyzed here.

The organization of this paper is as follows. We present our observing technique, data, and initial reduction in the next section, the analysis in Sect. 3, and the results in Sect. 4. Our main conclusion, discussed in Sect. 5, is that we find no evidence for spatial coincidence between internetwork K_{2V} grains and internetwork fields down to the limit set by the ASP sensitivity. There is also no obvious response of the Ca II chromosphere to horizontal internetwork field (HIF) events in the underlying photosphere. Taken together, these two results indicate that magnetic fields are not an essential ingredient for the production of K_{2V} grains.

2 Observations

The observations used in this paper were obtained on September 5 1996 with the Advanced Stokes Polarimeter (hereafter ASP; Elmore et al. 1992) at the Vacuum Tower Telescope of the National Solar Observatory/Sacramento Peak at Sunspot, New Mexico. The observations were part of a wider campaign to investigate chromospheric and coronal manifestations of disturbances in the photospheric magnetic field (SOHO Joint Observing Program 46) and focused on a very quiet area near solar disk center. It is shown in Fig. 4. In this paper we concentrate on the small internetwork area contained within the upper part of the narrow strip that is indicated at the center of the images of Fig. 4.

The ASP cameras were configured to observe the Zeeman-sensitive Fe I line pair at $\lambda = 630.15, 630.25$ nm

[2] Just north and west of the disk-center region studied in this paper, slightly enhanced network is found on co-temporal full-disk Ca II K images taken at NSO/Sacramento Peak.

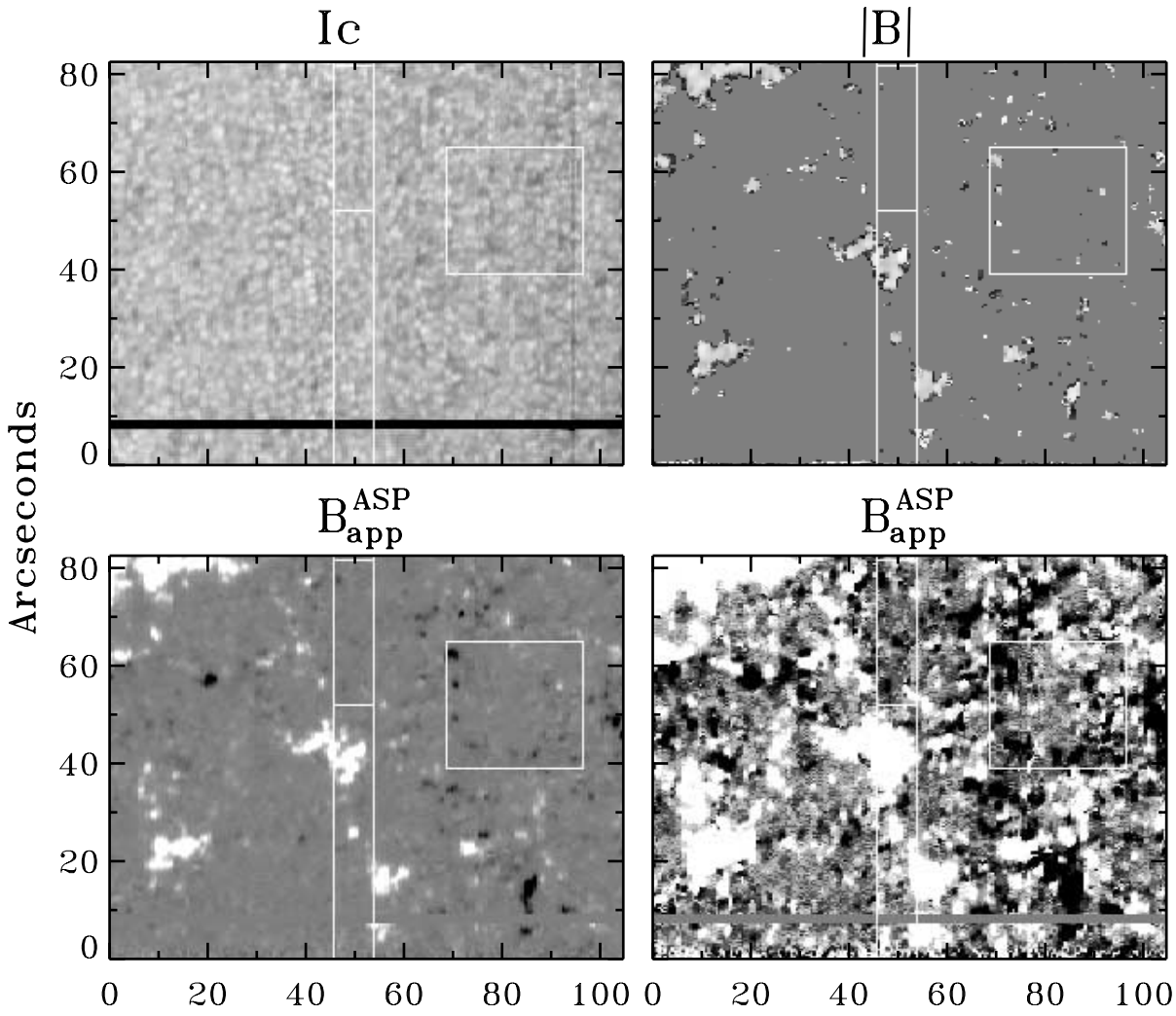

Figure 4: The spatial context of the time series data is revealed by this ASP map of a wider area during 13:55 - 14:12 UT on 1996 Sept. 5. The vertical lines near the center indicate the extent of spatial maps of the time series. The horizontal lines within delimit the very quiet internetwork area analyzed in detail. The rectangle at right defines a sub-area shown in Fig. 10. The I_c panel, from the continuum near $\lambda = 630$ nm, shows the photospheric granulation. The horizontal black bar is from a fiducial hair on the slit and the darkened column near $x = 95$ was probably caused by a miller moth *(Euxoa Auxiliaris [Grote])* in the light path. The grey scale of the upper right panel displays the intrinsic field strength $|\vec{B}|$ (bright = strong field) from the ASP inversion. No inversion was attempted for the uniform grey areas having $P_{\rm tot} < 0.003$ (Eq. 3). The selected internetwork area is field-free at this threshold. Bright areas mark network patches dominated by unresolved $|\vec{B}| \approx 1400$ Gauss flux tubes, having $B_{\rm app} \gtrsim 700$ Mx cm^{-2} (Eq. 4) and spatial fill fraction $f \gtrsim 0.5$ (cf. Fig. 8). The dark edges of network patches are probably spurious (see Sect. 3.3 of text). The bottom panels show the apparent flux density $B^{\rm ASP}_{\rm app}$ (Eq. 1) using the calibration relation shown in Fig. 8. The grey scale is clipped at $|B^{\rm ASP}_{\rm app}| = 174$ Mx cm^{-2} and $|B^{\rm ASP}_{\rm app}| = 14$ Mx cm^{-2} in the lower-left and lower-right panels, respectively, revealing "bloom" of network patches to large apparent size (cf. Fig. 7). Small areas of mixed-polarity weak magnetic flux, close to the noise limit of $|B^{\rm ASP}_{\rm app}| \simeq 3$ Mx cm^{-2} (see Fig. 9), are clearly visible in internetwork regions such as that within the rectangle at upper right, which is displayed in more detail in Fig. 10.

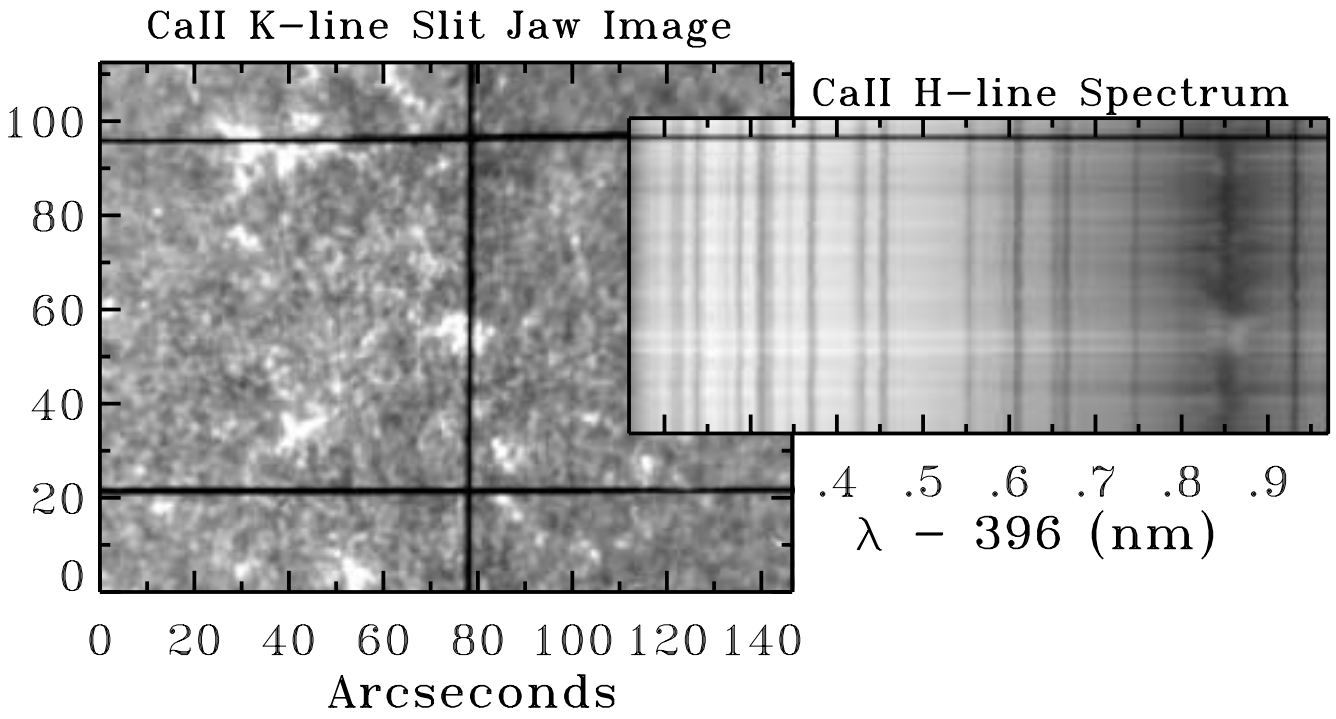

Figure 5: These Ca II H & K data show a slit-jaw filtergram (left) with a passband $\Delta\lambda = 0.3$ nm centered on Ca II K and the simultaneous, spatially aligned Ca II H spectrogram (right). The vertical dark line in the filtergram is the spectrograph slit and the two horizontal lines are fiducial hairs on the reflecting slit jaws. The grainy bright structure in the center of the slit-jaw field marks a cluster of strong-field chromospheric network elements which produce bright streaks throughout the observed segment of the spectrum. The dark region just above the network patch is the quiet internetwork area studied in detail.

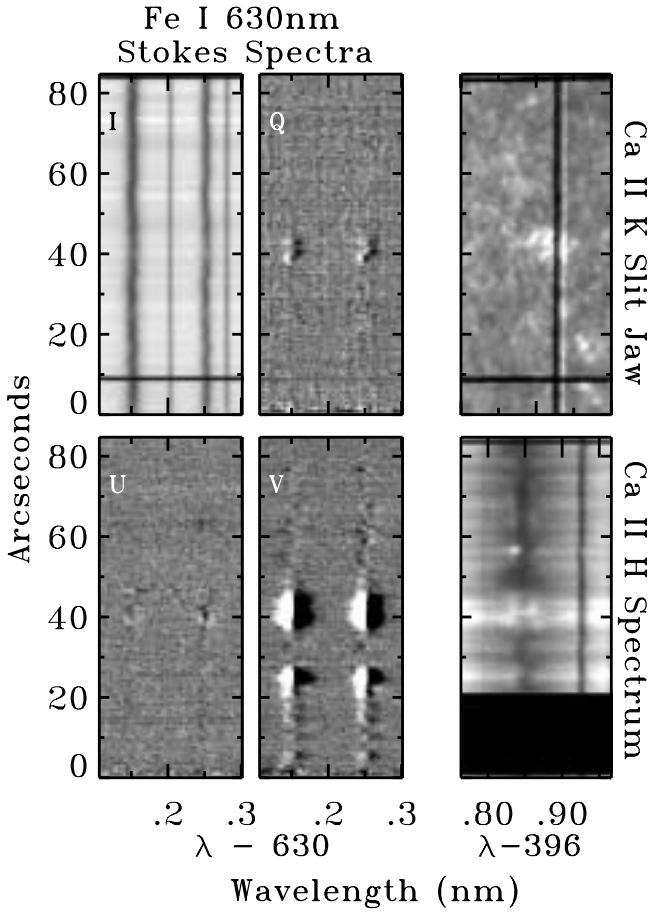

Figure 6: Shown in the four panels at left are ASP Stokes spectra of the Fe I 630.2 nm doublet at time $t = 37$ min and map position $x = 6$ arcsec in the time series. The grey scale of the Q and U panels is clipped at 0.2% of the continuum intensity I_c, and V is clipped at 0.4% I_c in order to emphasize weak polarization features. The Stokes Q panel shows slight crosstalk from the strong internetwork features in the Stokes V panel but no significant linear polarization elsewhere. The panel at upper right is a portion of the simultaneous Ca II K slit-jaw image shown in Fig. 5. The highlighted pixel column to the right of the dark slit indicates the slit position as seen by the ASP at 630 nm, displaced from the Ca II K slit position by the wavelength dependent refraction of the Earth's atmosphere. The panel at lower right shows a small spectral sample of Ca II H spectrogram corresponding to the offset slit position. The network elements around $y = 23$ arcsec and $y = 40$ arcsec produce bright emission throughout the Ca II H line core. The bright Ca II H_{2V} grain near $y = 57$ arcsec is accompanied by the typical dark redshifted H_3, dark H_{2R}, and bright wing "whiskers". It does not produce any obvious polarization signatures in the ASP panels. Interpolation of the Ca II H spectrograms to compensate for differential refraction results in images that are co-spatial but not exactly simultaneous with the ASP data.

in all four Stokes parameters (cf. Lites et al. 1993a; Lites et al. 1995). In addition, a camera from the NSO Multi-Diode Array (MDA) was placed in the focal plane of the spectrograph to register the intensity profile of the Ca II H resonance line at $\lambda = 396.8$ nm (cf. Balasubramaniam et al. 1997). The spectrograph was configured to project a relatively wide ($\Delta\lambda = 0.9$ nm) wavelength region on this camera, containing a large segment of the violet Ca II H wing in order to obtain spectral windows that range in formation height from the photosphere to the chromosphere. Sampling the photospheric "continuum" window in the far H-line wing permits accurate alignment of the H-line spectra with the simultaneous $\lambda = 630$ nm ASP data, including compensation for differential atmospheric refraction between the two wavelengths. This configuration resulted in spectral sampling of 2.014 pm/pixel (8th order) at $\lambda = 630$ nm and 4.035 pm/pixel (12th order) at $\lambda = 397$ nm. The 630 nm spectrograms have coarser sampling than the customary ASP 9th-order observations with 1.259 pm/pixel dispersion. The diffraction angle is also farther from the grating blaze. The ASP sensitivity was therefore slightly less than usual. The angular pixel size along the projected slit was 0.37 arcsec.

A second NSO-MDA camera registered the image reflected from the spectrograph slit through a $\Delta\lambda = 0.25$ nm wide Lyot filter centered on the Ca II K line at $\lambda = 393.3$ nm. These slit-jaw images were taken synchronously with the spectrograms. They display the location of the spectrograph slit in the field and the evolution of the chromospheric morphology during the observing sequence.

An example of a Ca II K slit-jaw image and the corresponding Ca II H spectrogram is shown in Fig. 5, and an example set of ASP data is shown in Fig. 6. The latter figure shows representative Stokes I, Q, U and V spectrograms in the four panels at left. The grey scale of the Q, U, and V panels is set to saturate at low values ("clipped") in order to bring out the weakest polarization features. The two panels at right show the simultaneous Ca II K slit-jaw image (top) and a segment near line-center of the corresponding Ca II H spectrogram (bottom). There is a prominent H_{2V} grain near $y = 57$ arcsec.

The time series data set analyzed below consists of co-spatial and co-temporal series of spectral ASP and Ca II H maps that were generated by stepping the 0.6×84.4 arcsec spectrograph slit repeatedly across an 10.5×84.4 arcsec area in 11 steps of 1.05 arcsec. The cameras took about one frame every six seconds during the period 14:16–15:25 UT; the average time interval between successive 11-step maps is 63.25 sec. The NSO correlation tracker (Rimmele et al. 1991) was used to stabilize the telescope image. It performed best during

the first 40 minutes, when the residual image excursions were small and when there was only a slow image drift. Later on, the drift accelerated and there were occasional interruptions when the tracker lost its lock on the solar granulation. We therefore analyze only the first 40 minutes of the time series data set here: a series of 38 ASP data cubes and 38 Ca II H data cubes, each consisting of maps per spectral resolution element, with accompanying Ca II K slit-jaw images.

During the twenty minutes prior to the time series data acquisition, the ASP executed a single-pass map over a ten times wider area around the 11 arcsec wide time series strip. This was done by stepping the slit 200 times incrementally over 0.525 arcsec. The results are shown in Fig. 4. The domain of the time series is indicated by vertical lines near the center of all panels. It contained a small patch of network at the center. The upper part included a very quiet internetwork area that is also indicated in each panel. We focus on this small internetwork area using the time sequence of ASP and Ca II data cubes to derive the space-time parameter charts that are shown in Figs. 11, 12, and 14–16. The network patch provided a convenient positional reference for compensation of the pointing drifts. Its relatively strong polarization signals and large intrinsic magnetic field strengths also provide a robust calibration of very weak observed Stokes V signals in terms of apparent flux density per pixel (Sect. 3.3 and Fig. 8).

3 Analysis

3.1 ASP – Ca II Alignment

The telescope guiding drifts were determined and corrected through cross-correlation of the successive net-polarization maps as constructed from the ASP data cubes. The network patches in the time series field provide sufficiently stable anchors for such pattern tracking.

The slit-jaw Ca II K images and the Ca II H spectrograms (including those in Fig. 6) have been spatially scaled, shifted, and interpolated to obtain spatial alignment with the corresponding ASP Stokes spectrograms. Differential refraction in the Earth's atmosphere causes a spatial offset between $\lambda = 396$ nm and $\lambda = 630$ nm. In the present data it has components of about 2 arcsec both along and perpendicular to the slit. These shifts were determined by cross-correlation of the quasi-continuum maps registered in the Ca II H wing window at $\lambda = 396.25$ nm with the ASP continuum maps measured near $\lambda = 630$ nm. The far-wing Ca II H window is formed sufficiently deep in the photosphere to enable such correlation. Exact alignment would have been more problematic had we recorded only the Ca II H core. The Ca II spectrograms have been shifted along the slit to compensate for the parallel component of the refractive offset. The displacement perpendicular to the slit was corrected through spectrogram interpolation among the 11 slit positions in each map of the sequence. The resulting alignment is significantly better than 1 arcsec.

The interpolated Ca II H spectrograms represent the same spatial location as the Stokes panels, but they are not strictly simultaneous with the latter, differing by a delay of about 6 - 12 s. This is sufficiently brief compared to the one-minute lifetime of H_{2V} grains. The MDA CCD recorded a smaller area than the ASP cameras as is evident in the lower part of the H_{2V} panel of Fig. 6. The Ca II K slit-jaw image at the upper right was taken simultaneously with the Stokes panels. The dark slit shows its actual position seen by the Ca II H spectrum, while the bright pixel column immediately to the right indicates the approximate slit position seen by the ASP at the time of this measurement.

3.2 Spectral Measurements

We have evaluated various parameters for each 0.37 arcsec spatial sample along the projected spectrograph slit for each set of simultaneous Ca II H and ASP spectrograms. From the Ca II H spectrograms (shifted and interpolated as described above) we measured some of the H-line intensity indices that are defined in Table 1 of Paper I: the H-index (0.1 nm wide band around line center), the H_{2R} and H_{2V} indices (0.008 nm around displacements from line center $\Delta\lambda = \pm 0.016$ nm, respectively), and the Doppler shift ratio $(H_{2V} - H_{2R})/(H_{2V} + H_{2R})$. The latter two quantities are not used in the present analysis.

From the ASP spectrograms we measured the total (signed) fractional (relative to I_c) Stokes V signal

$$V_{\rm tot} = \frac{\int_0^{\lambda_0} V(\lambda)\,{\rm d}\lambda - {\rm sgn}(V_{\rm blue}) \int_{\lambda_0}^{\infty} V(\lambda)\,{\rm d}\lambda}{I_c \int {\rm d}\lambda}, \qquad (1)$$

where ${\rm sgn}(V_{\rm blue})$ denotes the sign of the blue peak of the Stokes V profile of one of the two Fe I lines, the integration is over two passbands containing the two 630 nm lines, and λ_0 denotes the line center wavelength of the line being integrated. I_c is the continuum intensity near $\lambda = 630$ nm. In the limit of small $|\vec{B}|$ the amplitude of Stokes V scales linearly as the line-of-sight component of the field, $B_{\rm long}$ (see Chapt. 11 of Stenflo 1994), weighted by the fill factor f (Rabin 1992, see also Eq. (4) below.) The integral defining $V_{\rm tot}$ serves to increase the sensitivity to weak signals by averaging over many spectral samples.

Likewise, we determined the fractional net linear polarization

$$L_{\rm tot} = \frac{\int [Q^2(\lambda) + U^2(\lambda)]^{1/2}\,{\rm d}\lambda}{I_c \int {\rm d}\lambda} \qquad (2)$$

and the fractional net polarization

$$P_{\rm tot} = \frac{\int [Q^2(\lambda) + U^2(\lambda) + V^2(\lambda)]^{1/2}\, {\rm d}\lambda}{I_c \int\, {\rm d}\lambda}. \qquad (3)$$

The normalization implies that these total polarization measures are profile-averaged quantities. The integrals for $L_{\rm tot}$ and $P_{\rm tot}$ were carried out over the 630.25 nm line only.

In addition to these measurements, we applied the elaborate ASP inversion procedures described by Skumanich et al. (1997) at those space-time samples for which the polarization signals were sufficiently large to warrant detailed modeling of the Stokes profiles. The inversion algorithm delivers estimates of: the intrinsic field strength $|\vec{B}|$, the inclination of the field γ with respect to the local vertical ("zenith angle"), the spatial fill fraction f, other measures characterizing the line formation, and error estimates of each parameter of the fit to the Stokes profiles (Lites et al. 1994.) The meaning of f is discussed below.

3.3 ASP Polarization Analysis

Most of the network elements in this quiet region possess only small Stokes Q or U amplitude (cf. Fig. 6), indicating that the corresponding magnetic fields were aligned closely along the line of sight (vertical). Except for the occurrence of transient small-scale horizontal fields (HIFs) discussed below, the observed polarization in the internetwork part of the field is also dominated by Stokes V rather than Q or U. This is illustrated by the Stokes panels in Fig. 6, which show very little linear polarization (Q and U) even at enhanced sensitivity. Crosstalk of about $3-4\%$ from $V \rightarrow Q$ is evident as weak antisymmetric signal in the Q panel at the location of the network elements, indicating incomplete correction for telescope polarization. Because there were no sunspots available near disk center during our observing period, we have not been able to refine the telescope polarization model by the technique described by Skumanich et al. (1997) and we have therefore used an older model. The turret mirrors of the Vacuum Tower Telescope have been re-figured and re-aluminized since that earlier determination of the telescope Muller matrix. Because the turret mirrors cause most of the telescopic modification of the input polarization state, it is not surprising that the polarization model employed here is not optimal. However, residual instrument polarization in Stokes Q at the low level evident in Fig. 6 does not change any result below since 1) the network fields are primarily longitudinal, 2) a spurious antisymmetric signature in Stokes Q has no effect on the ASP inversion which assumes a symmetric profile, and 3) the transient HIFs discussed below are characterized by very weak Stokes V, such that any $V \rightarrow Q$ crosstalk is inconsequential.

The parameter f delivered by the ASP inversion algorithm is set largely by the fractional polarization $P_{\rm tot}$, whereas the vector field parameters $|\vec{B}|$ and γ are set largely by the relative amplitudes and profile shapes of $Q(\lambda)$, $U(\lambda)$, and $V(\lambda)$. It is important to appreciate that the fill fraction f is the dominant factor in setting the apparent flux density. It depends sensitively on the instrument and the (time-dependent) atmospheric seeing. Apparent flux densities are frequently quoted in the literature with the implicit suggestion that they are solar properties, or may be taken as such by unwary readers. In fact, apparent flux densities are instrument-dependent, and even observation-dependent. Figure 7 illustrates this for the case in which the observed solar area contains magnetic fields exclusively in the form of identical strong-field flux tubes — a case that is appropriate for unipolar network. Since the flux tube diameters are well below the effective angular resolution, their intrinsic polarization signatures consist of clusters of point sources. The observed apparent flux density then corresponds to a summed local sampling of multiple point spread functions, each centered at a flux tube location. The apparent flux density at a sample location may then be written as

$$B_{\rm app} = f\, |\vec{B}|\, \cos\gamma, \qquad (4)$$

where $|\vec{B}| = 1400$ Gauss and $|\cos\gamma| = 1$ in this idealized case. The dimension of $B_{\rm app}$ equals that of the intrinsic solar field strength (magnetic induction) $|\vec{B}|$, but following Keller et al. (1994) we use Mx cm^{-2} rather than Gauss for $B_{\rm app}$ in order to express its observation-dependent character. More specifically, we use $B_{\rm app}$ to designate flux density estimates that are based on detailed inversion modeling of Stokes I, Q, U, and V measurements, and we add appropriate labels such as ASP and BBSO to $B_{\rm app}$ for flux density estimates that are obtained magnetograph-wise from Stokes V alone. The fill fraction f quantifies the effect of the object convolution with the point spread function. The latter is generally dominated by atmospheric seeing and tends to possess extensive wings, far beyond the 1 arcsec halfwidth that corresponds to "good" seeing at most magnetograph sites. Thus, mapping the apparent flux density $B_{\rm app}$ at very high sensitivity, as is done below in order to display weak fields, causes the "bloom" extending outward from the strong polarization signals of network elements. The bloom results from seeing-diluted sampling of relatively distant kiloGauss fields.

If the intrinsic fields are unipolar and single-valued in $|\vec{B}|$ and γ within the entire area that contributes, via the point spread function, to the polarization signal at a given pixel (as in the hypothetical case of Fig. 7), the ASP inversion procedure yields estimates of $|\vec{B}|$ and $\cos\gamma$ that correspond closely to the intrinsic solar values. The

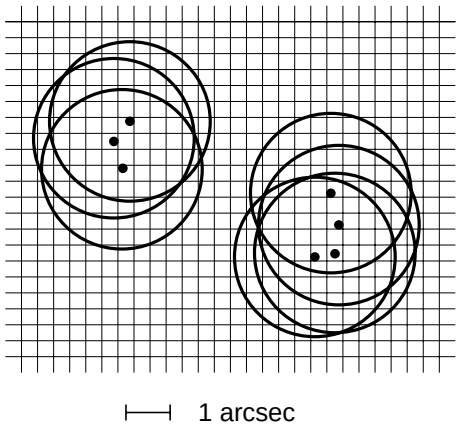

Figure 7: This cartoon illustrates ASP polarimetry of vertical, unipolar, $B = 1400$ Gauss flux tubes represented by dots of diameter 0.25 arcsec. The grid represents the 0.37 arcsec spatial sampling along the projected ASP slit. The large circles surrounding each dot represent smearing of the strong polarization signal from each flux tube due to scattering in the optics and atmospheric seeing, such that the blurred signal reaches the noise level of the observations at this radius (shown here as 5 spatial samples). Network elements "bloom" to apparent sizes of this order when polarization maps are displayed so as to reveal weak polarization (cf. Fig. 4).

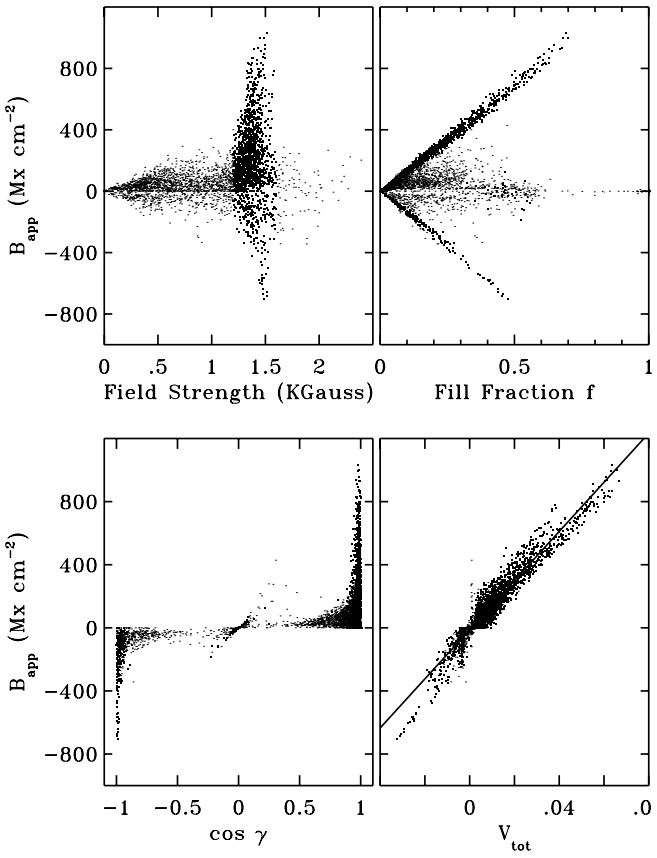

Figure 8: This figure illustrates the calibration of $|V_{\rm tot}|$ (Eq. 1) in terms of apparent flux density $B_{\rm app}$. The parameters $|\vec{B}|$, f, and $\cos\gamma$ plotted along the abscissae result from the ASP inversion of those locations in the map shown in Fig. 4 with total net polarization $P_{\rm tot} > 0.003$. The product $B_{\rm app} = f\,|\vec{B}|\,\cos\gamma$ plotted on the ordinates represents the apparent flux density measured in $\mathrm{Mx\,cm^{-2}}$. The samples with $1200 < |\vec{B}| < 1600$ Gauss, marked with slightly larger symbols, are dominated by $\cos\gamma \approx \pm 1$ and populate the two slanted linear relations in the upper right panel. These properties mark them as network fields, sampled at various levels of point-spread dilution as illustrated in Fig. 7. The remaining samples have small apparent flux density $B_{\rm app}$ and large scatter in the inferred values of $|\vec{B}|$, $\cos\gamma$ and f. They mark internetwork fields and the outer limits of diluted network polarization. The bottom right panel shows a fairly tight correlation between $B_{\rm app}$ and profile-averaged $V_{\rm tot}$, comprising both network and diluted network. The slope of the linear fit is used as a calibration constant to enable inference of apparent flux densities $B_{\rm app}^{\rm ASP}$ from $V_{\rm tot}$ at locations where the polarization is too weak for detailed Stokes profile inversion.

inferred fill fraction f then reflects the effective dilution of the polarization. Such analysis is limited ultimately by random noise, so that at very low signal, in the outer reaches of the point-spread disks, the inversion breaks down and yields large scatter in $|\vec{B}|$, γ, and f.

Figure 8 displays ASP inversion results for all 0.37×0.52 arcsec^2 spatial samples in Fig. 4 that have total net polarization $P_{\rm tot} > 0.003$; i.e. points for which the polarization exceeds the line-integrated noise level by about an order of magnitude. This threshold has been determined as necessary to achieve reliable fits to the Stokes profiles. The first three panels of Fig. 8 show a bimodal split into two categories. The samples with $1200 < |\vec{B}| < 1600$ Gauss (first panel) are plotted with larger symbols. With only a few exceptions, they fall within two tightly constrained linear branches obeying $B_{\rm app} \approx f\,B_0$ with $B_0 = \pm 1400\,$Gauss in the upper-right panel, and they cluster at $\cos\gamma = \pm 1$ in the lower-left panel. Clearly, these samples describe network fields with intrinsic field strength $|\vec{B}| \approx 1400$ Gauss, inclination $|\cos\gamma| \approx 1$ and fill fraction f that varies from small values up to about $f = 0.7$ according to resolution-smeared sampling as in Fig. 7. The second category of samples is characterized by small apparent flux density $B_{\rm app}$ and large spread in the model-fitted values of $|\vec{B}|$, $\cos\gamma$, and f. These points include both a few small patches of internetwork fields that have polarization greater than the threshold for inversion, and the outer edges of network point-spread disks where the inversion modeling breaks down. The former may be identified in the upper right panel of Fig. 4 as the few isolated, very small dark patches, whereas the latter are the dark borders surrounding the larger, lighter shade network patches.

Assuming that solar network flux tubes all have in-

trinsic field strength $|\vec{B}| \approx 1400$ Gauss, the network distributions in Fig. 8 may be compared to other observations. Figure 9 of Lin (1995) is directly comparable to the upper-left panel of Fig. 8. The scale along its y-axis is labeled "flux in Mx", but it actually measures apparent flux density $B_{\rm app}^{\rm BBSO}$ per 0.48 arcsec^2 spatial sample. The figure shows a similar peaked cluster centered at $|\vec{B}| = 1400$ Gauss, but it reaches only up to $|B_{\rm app}^{\rm BBSO}| \approx 100$ Mx cm^{-2} while the samples in our Fig. 8 reach $|B_{\rm app}| \approx 800$ Mx cm^{-2}. We attribute this factor-of-eight difference to the apparent fill fraction f, i.e., to difference in spatial resolution. Expressed in terms of seeing quality, it indicates that our angular resolution was nearly three times better. At lower values of $|\vec{B}|$, Lin's diagram shows a low-strength tail rather like the one in the upper-left panel of Fig. 8. The distribution seems similar, including slight clustering around $|\vec{B}| = 500$ Gauss.

A similar comparison is feasible with the two network field distributions plotted in Figs. 6–7 of Nindos & Zirin (1998). They reach up to only $B_{\rm app}^{\rm BBSO} \approx 30$ Mx cm^{-2} and $B_{\rm app}^{\rm BBSO} \approx 40$ Mx cm^{-2}, respectively, indicating yet lower angular resolution. Note that not only the seeing (integrated over as long as four minutes in the BBSO magnetogram acquisition) may contribute to this difference, but that also the sophistication of the modeling and other factors are important (cf. Lites et al. 1994; Zirin 1995; Lites 1996; Skumanich et al. 1997).

The final panel at the lower right in Fig. 8 is essential to the analysis of weak polarization in this paper. It shows that the apparent flux density $B_{\rm app}$ inferred by the inversion algorithm correlates closely with the profile-averaged circular polarization signal $V_{\rm tot}$ defined by Eq. (1). Since $V_{\rm tot}$ is measured with relatively high signal-to-noise resulting from the wavelength averaging over both line profiles, the good quality of this correspondence permits us to derive apparent flux densities $B_{\rm app}^{\rm ASP}$ from the measured $V_{\rm tot}$ at locations and times where the polarization falls considerably below the threshold needed for inversion of the Stokes profiles. The calibration relation indicated by the linear fit is $B_{\rm app}^{\rm ASP} = (15572 \pm 56)\, V_{\rm tot}$, with $B_{\rm app}^{\rm ASP}$ in Mx cm^{-2}. Its use permits us to construct complete $B_{\rm app}^{\rm ASP}$ maps and space-time charts, including also the areas with very weak polarization.

4 Results

4.1 Properties of Internetwork Fields

Nindos & Zirin (1998) separate network features from internetwork features in their observations at a "field strength" of about 10 Gauss. In view of the discussion above, this implies network/internetwork separation at an apparent flux density measured at BBSO on specific

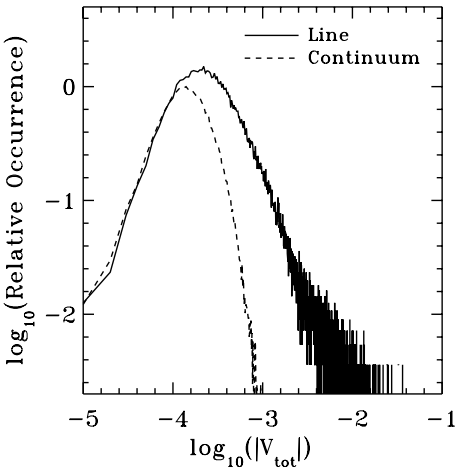

Figure 9: Histograms of the total Stokes V signal, $|V_{\rm tot}|$ as defined by Eq. (1), indicate the minimum useful polarization signals as limited by random noise in ASP measurements. The solid curve shows the frequency of occurrence of $|V_{\rm tot}|$ for all pixels of Fig. 4. The dashed curve is a similar histogram for Stokes V spectra integrated over an identical bandwidth, but shifted in wavelength to span only continuum having negligible polarization. This curve represents the noise distribution. It has been normalized to force coincidence of the downward slopes for $|V_{\rm tot}| < 2 \times 10^{-4}$, which are attributed to noise for both distributions (random noise reduces the likelihood of very small excursions). The noise level of the $V_{\rm tot}$ is estimated from the location (first moment) of the peak of the dashed curve: $|V_{\rm tot}| = 2 \times 10^{-4}$.

days of about $|B_{\rm app}^{\rm BBSO}| = 10$ Mx cm^{-2}. Can we set a similar dividing value? The locations with maximum $|B_{\rm app}|$ in our data undoubtedly describe network fields, but even these do not portray individual magnetic elements but rather unresolved element clusters as evident in the G-band panel of Fig. 2[3]. Our samples with smaller apparent flux density $|B_{\rm app}|$ either correspond to true internetwork fields, or represent the blurring of nearby flux tubes in the neighborhood of network patches. Even where we measure $|B_{\rm app}| < 10$ Mx cm^{-2} the signal may yet be caused by distant strong-field network. This is demonstrated below (Fig. 13). Thus, network/internetwork discrimination is not feasible by setting a single $|B_{\rm app}|$ dividing value. The internetwork area studied here, as outlined in Fig. 4, was selected by inspection of the slit-jaw Ca II K movie. On such movies the network patches stand out as being relatively stable amidst the rapid pattern changes caused by the apparently supersonic motions that the internetwork brightenings display. The H_{2V} space-time charts in Fig. 12 indeed confirm that the selected region contains no network since there are no bright streaks that

[3]Or for a much larger field on the high-resolution La Palma poster available at URL http://diapason.lmsal.com/~berger/images/gallery.html.

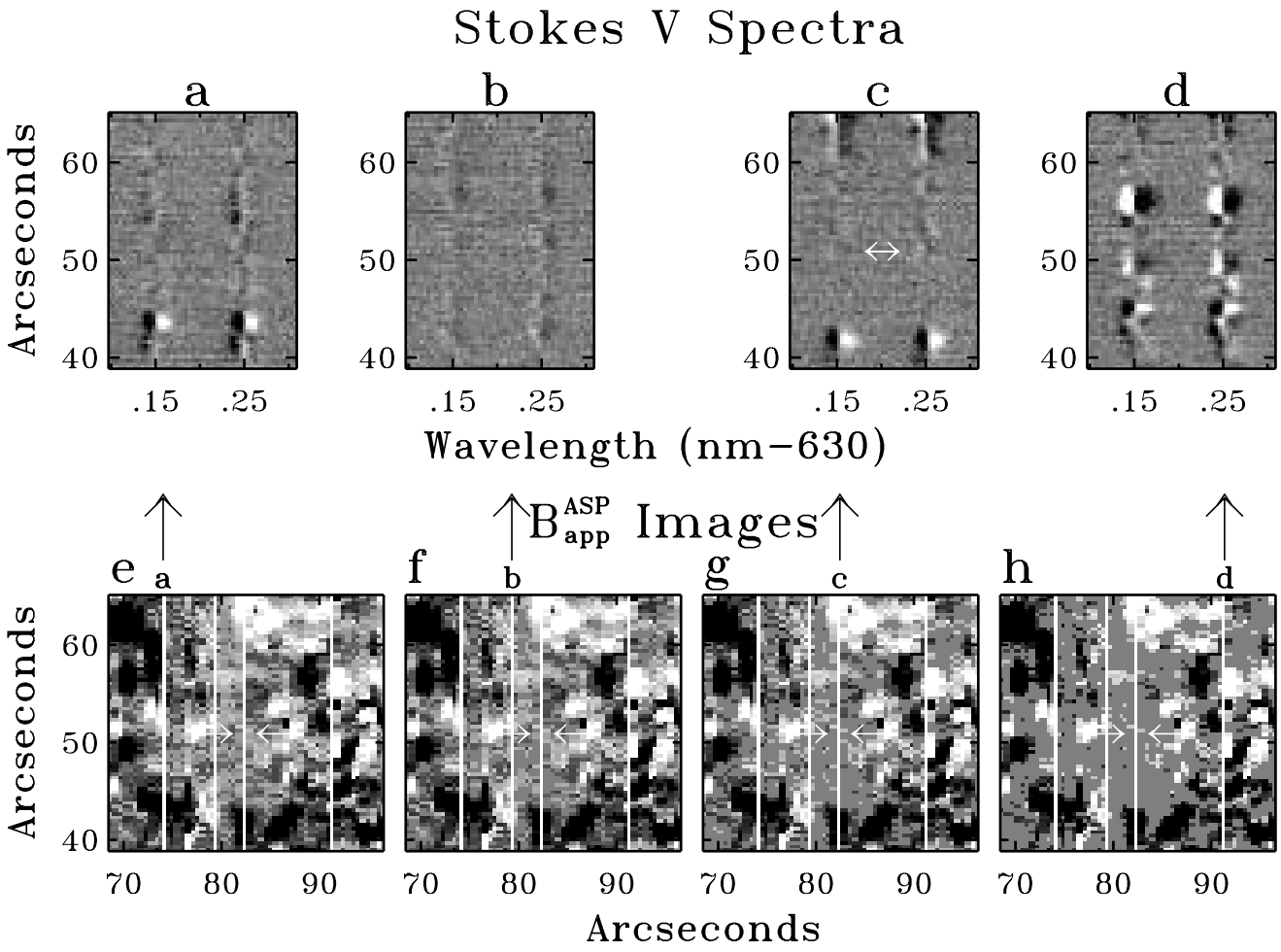

Figure 10: Spectropolarimetry of a very quiet internetwork region at the upper right of Fig. 4 emphasizes properties of weak flux. The upper panels are individual Stokes V spectrograms corresponding to the four slit positions highlighted in the spatial maps below, as identified by alphabetic labels and arrows. The grey scale displays Stokes V in the range $|V| \leq 0.003\ I_c$. The lower panels show maps of the apparent flux density $B^{\rm ASP}_{\rm app}$ at very high sensitivity and various values of lower threshold: 0, 3, 4.5, and 6 Mx cm^{-2} for panels e, f, g, and h, respectively. $B^{\rm ASP}_{\rm app} = 6$ Mx cm^{-2} corresponds to $|V_{\rm tot}| = 0.0004$. The horizontal arrows in spectrogram c and all $B^{\rm ASP}_{\rm app}$ images indicate a very weak Stokes V feature near the noise limit of the observations.

persist during 40 min. The apparent flux densities in this area (in the scale of our particular data set!) remain below $|B_{\rm app}^{\rm ASP}| \approx 40$ Mx cm^{-2} (Fig. 13).

Next we consider the lower cutoff for $B_{\rm app}$. When the line polarization falls below the noise level, the estimation of $B_{\rm app}^{\rm ASP}$ from $V_{\rm tot}$ via the calibration relation of Fig. 8 breaks down. Because we have spectral measurements containing continuum that is effectively devoid of solar polarization, we are able to use this continuum to establish a definitive measure of the noise in $V_{\rm tot}$. The lower threshold of validity is revealed in the histogram indicated by the solid curve in Fig. 9, which shows the occurrence distribution of $V_{\rm tot}$ over the full map in Fig. 4. The histogram shows a peak around $\log_{10}|V_{\rm tot}| = -3.7$. We attribute the rapid decline at smaller values of $|V_{\rm tot}|$ to random noise which inhibits the occurrence of small $V_{\rm tot}$. At these ASP signal levels, Stokes V is limited by the statistics of photon detection. We quantify the threshold by adding a second histogram (dashed curve in Fig. 9) that is determined in the same fashion as the solid curve, but measured for the continuum rather than a line. The bandwidth of the spectral average of Stokes V represented by the dashed curve is identical to that of the $V_{\rm tot}$ integration in Eq. (1). This histogram represents the noise distribution since the continuum has negligible circular polarization. Its peak location provides an estimate of the noise threshold in our polarization data: the first moment suggests that values $|V_{\rm tot}| > 2 \times 10^{-4}$, or correspondingly $|B_{\rm app}^{\rm ASP}| > 3$ Mx cm^{-2}, are significant. This noise limit is slightly worse than the customary sensitivity of the ASP in its standard mode of operation and at excellent seeing. The present data have lower signal-to-noise due to the larger spectral dispersion (2.014 pm/pixel instead of 1.259 pm/pixel), the larger departure from the grating blaze, and the somewhat coarser angular resolution (about 1.5 arcsec seeing, instead of 1 arcsec or even better).

We now consider to what extent "salt-and-pepper" internetwork fields as described by Livingston & Harvey (1971) and Harvey (1977) are detectable in our data. This issue is addressed by Fig. 10. The upper panels show sample Stokes V spectrograms for the quiet subfield outlined by the rectangle at the upper right of Fig. 4. The lower panels show the corresponding $B_{\rm app}^{\rm ASP}$ map of this area produced through the calibration relation of Fig. 8. The map is displayed four times for progressively higher thresholds: Panel e, without threshold, is simply an enlargement of the rectangle in the fourth panel of Fig. 4; panels f, g, and h have thresholds set to $|B_{\rm app}^{\rm ASP}| = 3$, 4.5, and 6 Mx cm^{-2}, respectively. The feature crowding diminishes from left to right because the weaker features vanish into the grey threshold. Our noise estimate derived from Fig. 9 indicates that all non-grey features in the two maps at right should be significant, whereas the two panels at left should contain appreciable random noise in addition to solar features. Furthermore, noise varies spatially from pixel-to-pixel, whereas solar polarization is limited to areas of at least several pixels due to seeing and actual solar clustering of weak flux.

Comparison with the sample Stokes V spectrograms in the upper panels enables verification of the significance of the features in the lower panels of Fig. 10. Slit positions for each spectrogram are indicated by bright columns in the maps, each labeled with the corresponding spectrum panel designation. Stokes V spectral features may be identified with their $B_{\rm app}^{\rm ASP}$ signature. For example, the strong Stokes V signal around $y = 43$ in spectrogram a is due to a weak, negative polarity network patch appearing as an isolated feature in $|\vec{B}|$ and $B_{\rm app}^{\rm ASP}$ of Fig. 4. In spite of its weakness, it is saturated in the lower panels of Fig. 10, exceeding the $|B_{\rm app}^{\rm ASP}| = 47$ Mx cm^{-2} upper limit (corresponding to a clipping value $|V_{\rm tot}| = 0.003$). The four diffuse, weaker patches of positive Stokes V signal in spectrogram b produce corresponding weak, but brighter-than-grey features at slit location b, the cores of which survive the threshold $|B_{\rm app}^{\rm ASP}| > 6$ Mx cm^{-2} for panel h. The double arrow in spectrogram c at $y = 51.5$ and in all lower panels identifies a diffuse and very weak feature with barely detectable yet significant Stokes V spectral signature. The $B_{\rm app}^{\rm ASP}$ measurement is a pixel-by-pixel process which does not utilize any information from adjacent pixels, but visual inspection picks up the presence of this feature in panels e and f because of its larger spatial signature. Inspection of panel c clearly reveals its presence thanks to the visual pattern recognition of the distinctive antisymmetric Stokes V spectral signature that is present over several pixels and in both lines.

Are there locations in this internetwork area that are truly field-free? Inspection of the upper panels of Fig. 10 indicates that there are locations without discernible Stokes V signature, for example below the double arrow in panel c. Given our noise limit, we can only conclude that $|B_{\rm app}^{\rm ASP}| < 3$ Mx cm^{-2} at these places. However, there is an increase in the spatial occurrence of single-polarity patches with 2–5 arcsec sizes from right to left in the bottom panels. Similar patches are also seen in other parts of the lower right panel of Fig. 4. Since their sizes seem to exceed the coincidences of a very few pixels expected for random noise, we suspect that smaller flux concentrations than $|B_{\rm app}^{\rm ASP}| \approx 3$ Mx cm^{-2} do exist.

4.2 H_{2V} Grains versus Internetwork Fields

We now turn to the issue of internetwork grain–magnetic field correlation. Figure 11 shows examples of the H_{2V} index (upper panels) and the apparent flux density $B_{\rm app}^{\rm ASP}$ (lower panels) derived from the time sequence of maps. The narrow panels at the left are in-

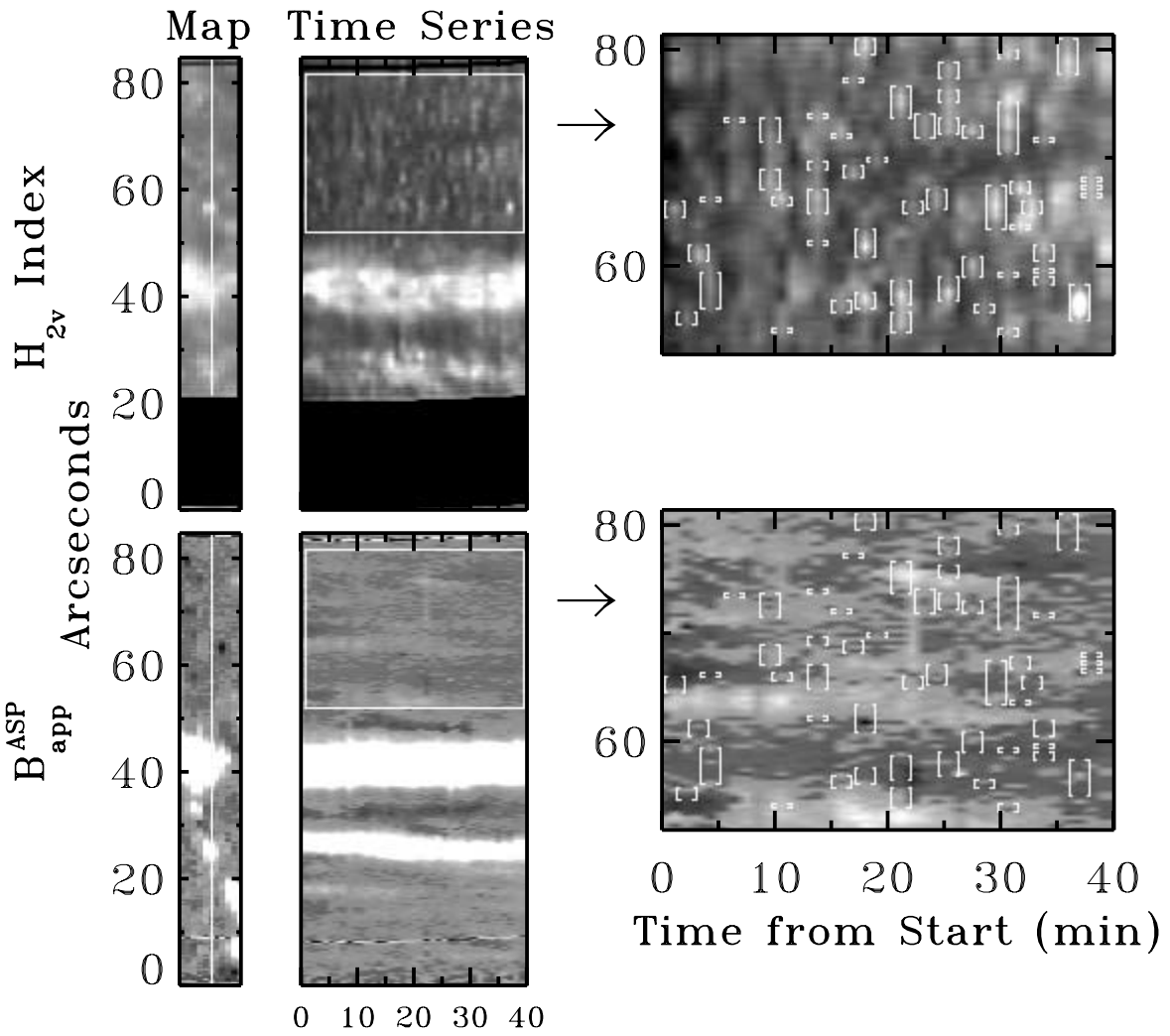

Figure 11: A comparison is shown between Ca II H_{2V} brightness modulation and apparent magnetic flux density $B_{\rm app}^{\rm ASP}$ for the sequentially mapped region outlined in Fig. 4. One map obtained at $t = 37$ min is shown in the panels at left. The upper left map shows the H_{2V} index (Sect. 3.2.) The lower left map shows the corresponding apparent flux density $B_{\rm app}^{\rm ASP}$ on a grey scale clipped at ± 50 Mx cm^{-2}. The middle column displays the evolution of the H_{2V} index and $B_{\rm app}^{\rm ASP}$ for the slit position highlighted in the left panels, at the same scale as the images on the right. The bright Ca II H_{2V} grain at $y = 57$ arcsec at left is seen at $t = 37$ min in the H_{2V} space-time chart and is also shown in Fig. 6. The internetwork sub-area outlined in Fig. 4, as highlighted in the middle columns, is enlarged in the right column. The upper right shows three-minute H_{2V} modulation. The brightest of these events are bracketed in the enlarged space-time charts, and the same brackets overlie the enlarged $B_{\rm app}^{\rm ASP}$ chart at lower right. The grey scale of that image ranges from -16.7 to $+22.2$ Mx cm^{-2}. It reveals no obvious spatial alignment of the bright H_{2V} locations with magnetic field enhancements.

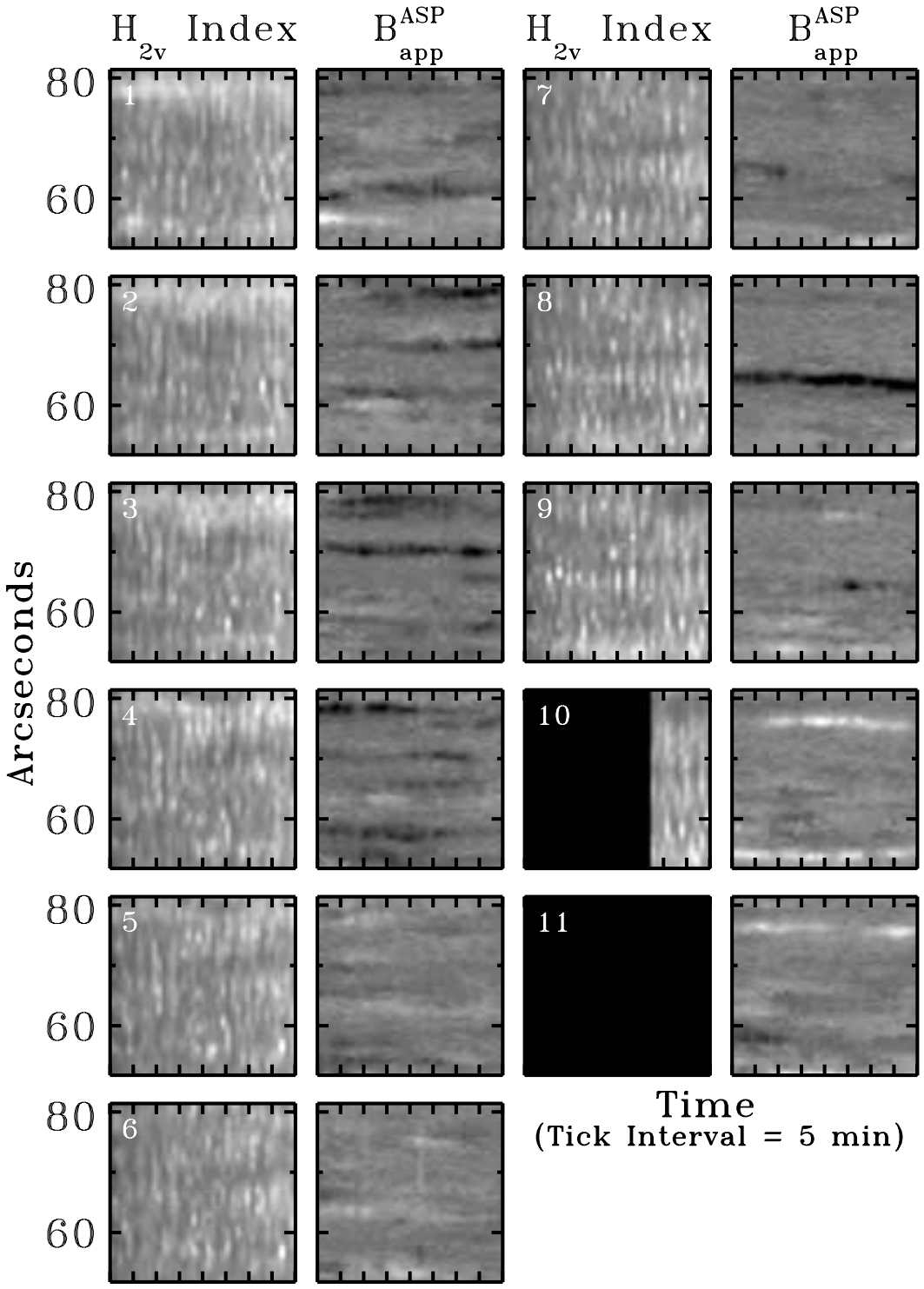

Figure 12: Space-time chart pairs for the internetwork region are shown for each of the eleven spatial positions of the spectrograph slit in the time series of maps. In each panel, horizontal is time and vertical is the spatial distance along the slit. The spatial step between slit positions is 1.05 arcsec. The left column of each pair shows the H_{2V} index (see Sect. 3.2), identified by slit position at upper left. The panel pair for slit position $x = 6$ is enlarged in Fig. 11. The right columns show apparent flux density $B^{\rm ASP}_{\rm app}$. The grey scale is clipped at $|B^{\rm ASP}_{\rm app}| \leq 40$ Mx cm^{-2}. The H_{2V} charts for slit positions $x = 10$ and 11 are incomplete due to the differential refraction between the two wavelengths.

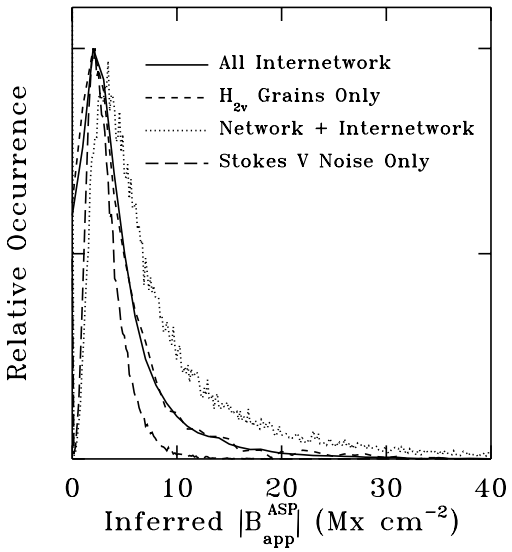

Figure 13: Histograms of $|B_{\rm app}^{\rm ASP}|$, comprised of the internetwork space-time charts of Fig. 12 show no distinction of the distribution for grains. The solid curve is the distribution for every pixel of charts 1 – 9, and the dashed curve represents the distribution for only the H_{2V} excess locations such as those identified by the brackets in in Fig. 11. The dotted and long-dashed curves are the same as in Fig. 9 and describe the full-field $|B_{\rm app}^{\rm ASP}|$ distribution and the Stokes $|V|$ continuum fluctuations, respectively.

dividual maps of these two quantities, constructed from the eleven-position slit map taken about 37 minutes after the beginning of the map sequence. The H_{2V} map is truncated at the bottom due to the limited field-of-view of the MDA detector and at the right due to differential refraction. The bright pixel columns indicate the slit position for which the space-time charts of the middle and right panels were derived. These cover the entire time sequence for this slit position, which was selected for this display because it contains the bright H_{2V} grain at $y = 57$ arcsec and $t = 37$ min. This grain is also visible in the Ca II H spectrogram of Fig. 6. The lower cutoff of the H_{2V} chart is curved due to the correction for slow drift of the field along the slit (Sect. 3.1).

The internetwork region outlined in Fig. 4 is indicated by a highlighted box in the space-time charts of the middle panels, which in turn are enlarged in the panels at right. The H_{2V} panel displays modulation that is characteristic of the chromospheric three-minute oscillation (cf. Fig. 4 of Rutten 1994; Fig. 6 of Rutten 1995). The brackets were defined by application of a median filter to this space-time chart in order to locate local maxima of the H_{2V} index. These brackets also overlie the corresponding expanded $B_{\rm app}^{\rm ASP}$ space-time chart. There is no obvious association of H_{2V} brightenings with either localized field excesses or with field deficits. Note that the grey scale for the enlarged display ranges over $-16.7 \leq B_{\rm app}^{\rm ASP} \leq 22.2$ Mx cm^{-2} (the extrema of variation of this internetwork region) so that this comparison is a highly sensitive one, emphasizing the very weakest fields down to the $|B_{\rm app}^{\rm ASP}| \approx 3$ Mx cm^{-2} noise limit.

Figure 12 displays the H_{2V} — $B_{\rm app}^{\rm ASP}$ internetwork space-time comparisons for all eleven spectrograph slit positions comprising the time series of maps. There are a few coincidences, most noticeably at slit position $x = 8$ where the slowly drifting negative polarity feature in the $B_{\rm app}^{\rm ASP}$ panel seems to be accompanied by slowly increasing H_{2V} brightness, and possibly by enhanced H_{2V} grain activity in the first half of the adjacent $x = 9$ panel. This magnetic feature peaks at $B_{\rm app}^{\rm ASP} = -55$ Mx cm^{-2}; its distribution along the slit has a FWHM of 1 arcsec. It appears to be confined to the $x = 8$ slit position, so that its total magnetic flux is less than 3×10^{17} Mx. Its possible association with H_{2V} grain activity peaking at $x = 9$ may make it an "internetwork flasher" similar to that of Brandt et al. (1992, 1994) and the three features marked in Fig. 2. However, considering the entire ASP data set, there is certainly no one-to-one spatio-temporal correlation between H_{2V} brightenings and flux density enhancements as was claimed by Sivaraman & Livingston (1982). In particular, the brightest H_{2V} grains such as the ones in panels $x = 2-3$ and $5-7$ do not show obvious magnetic connections at the ASP sensitivity.

Further evidence for lack of correlation between H_{2V} brightness excess and enhanced vertical field strength in the internetwork domain is provided by the solid and dashed histograms in Fig. 13. These histograms differ from those of Fig. 9 in that $|V_{\rm tot}|$ is converted to $|B_{\rm app}^{\rm ASP}|$, and that only the internetwork region of the sequentially mapped area is considered. The solid curve specifies the distribution over all internetwork space-time samples, whereas the short-dashed curve represents the partial distribution over only the "H_{2V} grain" locations having chromospheric H_{2V} brightness excess as bracketed in Fig. 11. Significant departure between the two curves would be expected for any association between H_{2V} brightness excess and magnetic flux. However, the two distributions are virtually identical.

The other two curves in Fig. 13 measure the distribution of $|B_{\rm app}^{\rm ASP}|$ and the Stokes $|V|$ continuum fluctuations over the full field of Fig. 4. They are the same as in Fig. 9 but are presented on the linear $|B_{\rm app}^{\rm ASP}|$ scale and are normalized to the same peak height as the internetwork histograms. The lower (long-dashed) curve, representing random noise, falls well below the internetwork distribution. The upper (dotted) curve includes the network patches in the full field and falls well above the internetwork distribution at these small values of $|B_{\rm app}^{\rm ASP}|$. This departure is a result of seeing and instrumental scatter from strong but distant flux tubes, show-

ing once again that one cannot define a specific value of $|B_{\rm app}^{\rm ASP}|$ as a network/internetwork discriminator. For $|B_{\rm app}^{\rm ASP}| < 2$ Mx cm^{-2} the histograms from the sequentially mapped region (solid, dashed curves) present a much larger occurrence of very small polarizations due both to the larger bin size of these histograms and, more importantly, to the effect of spatio-temporal interpolation between adjacent $V_{\rm tot}$ samples of opposite sign.

4.3 Properties of Horizontal Internetwork Fields

We now turn to the horizontal internetwork fields (HIFs) discovered by Lites et al. (1996). These are very small, transient appearances of predominantly horizontally oriented magnetic flux that tend to be accompanied by blueward Doppler shifts. Because small dynamic events in the photosphere may produce much more dramatic phenomena higher up, we thought it worthwhile to search for an association between HIFs and H_{2V} grains. This is done in Figs. 14–16. We first compare the HIFs with the longitudinal fields in the internetwork.

Figure 14 displays space-time charts of $L_{\rm tot}$ and $B_{\rm app}^{\rm ASP}$ in the format of Fig. 12 for all slit positions covering the sequentially mapped internetwork region. Locations of enhanced linear polarization with $L_{\rm tot} \geq 0.00073$ (i.e., HIFs) are highlighted in the adjacent $B_{\rm app}^{\rm ASP}$ panels. Some are labeled alphabetically. HIF event *d* in the 9th panel pair of Fig. 14 is also shown in Fig. 15.

The scarcity and the transient nature of the HIF events is striking when compared with the persistence of the stronger Stokes *V* features. The latter produce long-duration dark and bright streaks in the $B_{\rm app}^{\rm ASP}$ panels that often extend over $2-3$ arcsec into the neighboring panels for adjacent slit positions, while most HIFs measure only 1 arcsec or less. A few HIF events might coincide with the appearance or disappearance of bipolar features in the $B_{\rm app}^{\rm ASP}$ space-time charts. In particular, the HIFs identified in Fig. 14 by *b* and *c* at slit positions $x = 4$ and $x = 6$ seem to occur at the initial spreading of two very weak opposite-polarity Stokes *V* features, suggestive of the emergence of new flux, whereas HIF *d* in panel 9 seems to lie at the coalescence and cancellation of a very weak bipolar *V* feature pair. Lites et al. (1996) speculated that HIFs may mark flux emergence sites. These data do not confirm this suggestion conclusively but hint that it may be partially the case.

4.4 H_{2V} Grains versus Horizontal Internetwork Fields

Finally, we test the possibility that H_{2V} grains coincide (possibly at some time delay) with locations where HIFs occur in the underlying photosphere. Figure 15 shows ASP Stokes spectrograms in which HIF event *d* in Fig. 14 is prominent, especially in Stokes *U*. The panels at the right of the figure show corresponding spatial maps and space-time charts for H_{2V} brightness, linear polarization $L_{\rm tot}$ and the apparent flux density $B_{\rm app}^{\rm ASP}$. The arrow in each panel indicates the HIF space-time location. The brightness peaks in the H_{2V} space-time chart (upper right) are again indicated by bracket pairs that are also overlaid on the $L_{\rm tot}$ and $B_{\rm app}^{\rm ASP}$ charts. Figure 16 displays similar comparisons for all slit positions. There is no obvious correlation between the occurrence of H_{2V} grains and HIFs, even considering time delays. In addition, the HIFs are smaller than the H_{2V} brightenings and occur much less frequently.

5 Discussion

We have found no clear correlation between the occurrence of internetwork grains as evidenced by Ca II H_{2V} brightenings and the presence of internetwork Stokes *V* features with apparent flux density above our $|B_{\rm app}^{\rm ASP}| \approx 3$ Mx cm^{-2} noise threshold. We have also not found direct correspondence between internetwork grains and HIFs.

The first result contradicts the claim of Sivaraman & Livingston (1982) that Ca II K_{2V} grains are co-located one-to-one with internetwork field enhancements, and further that they obey a qualitative correlation between brightness and apparent flux density (that they denote as "field strength"). We believe that our higher angular resolution, the narrower Ca II passband used here, the synchronicity of our polarimetry and Ca II H spectrometry, and the overall quality of the ASP as well as its reduction procedures combine to make this conclusion quite robust. Indeed, the flux density histogram in Fig. 2 of Sivaraman & Livingston (1982) peaks near $|B_{\rm app}^{\rm KPNO}| = 15$ Mx cm^{-2}, indicating a noise level of this order although they claim a "background" of about 5 Mx cm^{-2}. Its tail extends to $|B_{\rm app}^{\rm KPNO}| > 70$ Mx cm^{-2}, while the internetwork tail in our Fig. 13 does not reach $|B_{\rm app}^{\rm ASP}| = 40$ Mx cm^{-2}. Since we are confident that our angular resolution is much better, we suspect that their extended tail betrays the inclusion of network fields and that these have contributed to the apparent one-to-one correspondence.

The second result, absence of $H_{2V}-$HIF correspondence, does not exclude that HIFs possess a chromospheric signature, nor does it establish their nature. As noted by Lites et al. (1996), these small transient features tax the limits of ASP capability. Significant advances in polarization sensitivity, angular resolution, temporal and spatial coverage are needed to improve on these. Because the polarization is small in the visible, infrared spectropolarimetry may present a more sensitive diagnostic of these features.

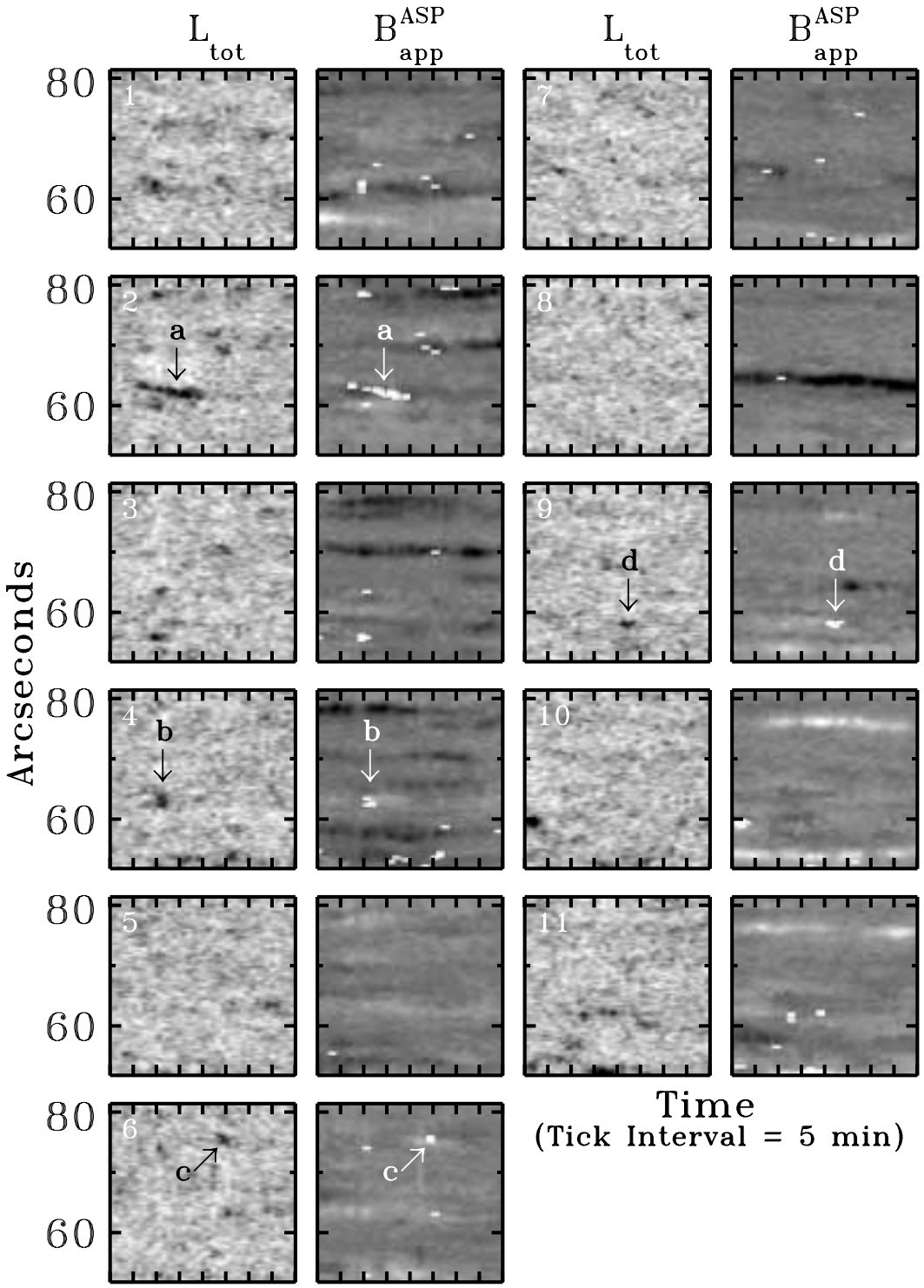

Figure 14: Locations of HIF (horizontal internetwork field) events in the internetwork region are compared in the format of Fig. 12 to the evolution of the apparent flux density. Space-time chart pairs for the internetwork region are shown for all eleven spatial slit positions. The left image of each pair shows the profile-averaged linear polarization $L_{\rm tot}$. The grey scale is clipped at $0.0004 \leq L_{\rm tot} \leq 0.0008$ and the sign is reversed so that large linear polarization appears dark. The right panel of each pair shows the apparent flux density $B_{\rm app}^{\rm ASP}$ with the grey scale clipped at $|B_{\rm app}^{\rm ASP}| \leq 40$ Mx cm^{-2} (same as $|B_{\rm app}^{\rm ASP}|$ in Fig. 12 but with HIF events highlighted.) Various HIF events are marked alphabetically in the left panels and all HIF events are highlighted in the right panels.

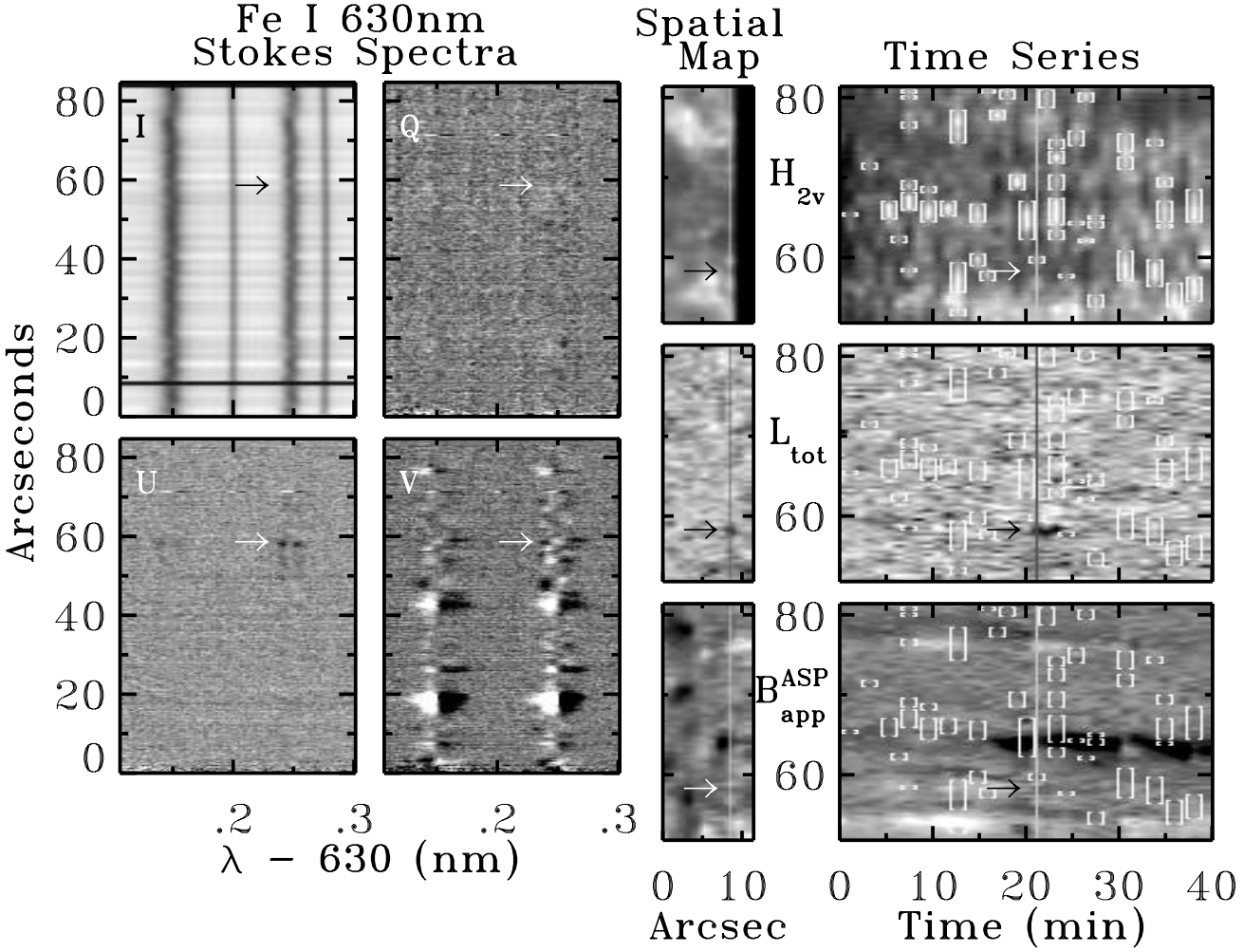

Figure 15: A HIF event is compared to the observed Ca II H brightness. The arrow in each panel indicates the space-time location of the HIF. The four panels at left show ASP Stokes spectra for slit position $x = 9$ arcsec and time step $t = 21$ min. The three panels in the middle present spatial maps at $t = 21$ min. Panels on the right are space-time charts of the internetwork region for the H_{2V} index (top), the profile-averaged net linear polarization $L_{\rm tot}$ (middle), and the apparent flux density $B_{\rm app}^{\rm ASP}$ (bottom) corresponding to the highlighted slit position in the maps, and also to the Stokes spectra. The brackets in the space-time charts specify the locations of H_{2V} brightenings derived for the top chart. The highlighted pixel columns (bright or dark) in the panels at right indicate times for which the maps in the middle panels are displayed. The displays for $L_{\rm tot}$ have been sign-reversed so that large polarization appears dark. The grey scales are clipped at ± 0.002 for the Q, U, and V Stokes spectra, at $0.0004 \leq L_{\rm tot} \leq 0.0008$ for the $L_{\rm tot}$ panels, and at $|B_{\rm app}^{\rm ASP}| \leq 20$ Mx cm^{-2} for the $B_{\rm app}^{\rm ASP}$ panels.

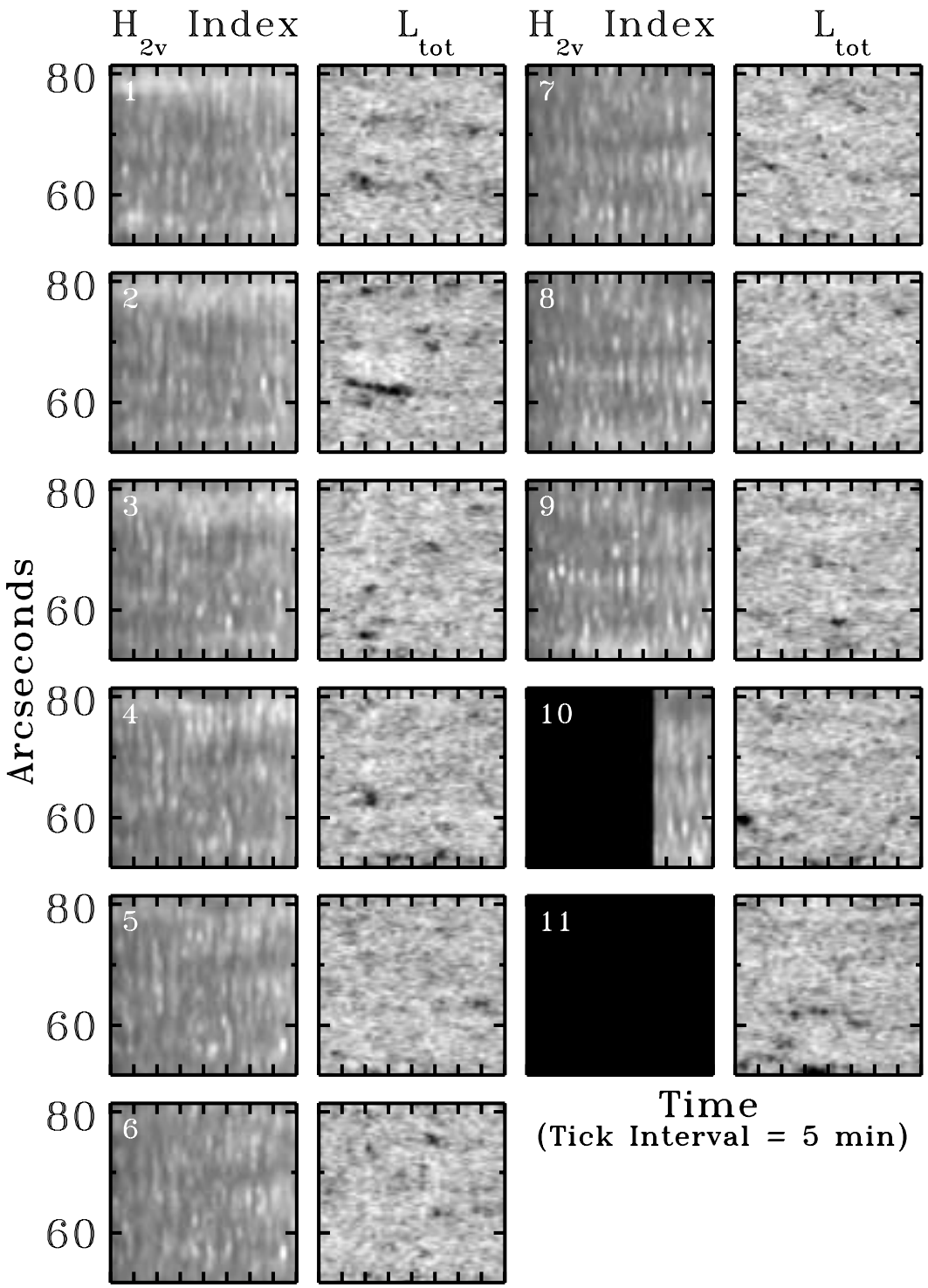

Figure 16: H_{2V} intensity modulation is compared to HIF events for all slit positions. The left columns show H_{2V} space-time charts as in Fig. 12, and the right columns show $L_{\rm tot}$ space-time charts as in Fig. 14. There is no obvious correlation between H_{2V} brightenings and HIF events.

Finding that the occurrence of internetwork grains, apart from the rare persistent flashers, does not depend on magnetism raises the question whether there are other phenomena that act as specific pistons for grain excitation. On the basis of other work we suspect that sudden convective down flows at or just below the surface that seem to produce "acoustic events" and "intergranular holes" may also enhance grain production in the overlying chromosphere (cf. Restaino et al. 1993; Rimmele et al. 1995; Rast 1995; Roudier et al. 1997; Hoekzema & Rutten 1998; Hoekzema et al. 1998; Goode et al. 1998).

6 Conclusions

We have supplied yet more evidence that the occurrence of most Ca II K_{2V} and H_{2V} grains in solar internetwork regions does not depend on the presence of magnetic fields. Whether their occurrence marks specific piston locations with future diagnostic value remains an open question. Answering this question may become both easier and more important now that the ultraviolet images from the TRACE mission mission[4] display internetwork grains similar to those in K_{2V} and H_{2V}. In the future, the planned Solar-B mission may enable measurements as presented here without the handicap imposed by the Earth's atmosphere.

We thank Fritz Stauffer at NSO/Sacramento Peak for software to synchronize the MDA and ASP exposures and the observers at the NSO/SP Tower Telescope, S. Hegwer, D. Gilliam, and B. Armstrong for their expert assistance in setting up and running the ASP. Furthermore, we thank D. Elmore and K. Streander of HAO for assistance at NSO during this observing run. We thank H. Peter for suggesting many improvements to the manuscript. RJR is indebted to HAO and LMSAL for hospitality. BWL was supported in part by NASA SOHO Guest Investigator Award W-19,328. TEB was supported by NASA contract NAS8-39747 (SOHO/MDI) and Lockheed-Martin Independent Research Funds. RJR's travel to LMSAL was partially supported by NASA SR&T Grant NASW–98008.

References

Athay R. G. 1970, Solar Phys., 11, 347
Balasubramaniam K. S., Keil S. L., Tomczyk S. 1997, ApJ, 482, 1065
Beckers J. M., Artzner G. 1974, Solar Phys., 37, 309
Berger T. E. 1997, Observation and Analysis of Small-scale Solar Magnetic Structure, PhD thesis, Stanford Univ.
Berger T. E., Loefdahl M. G., Shine R. S., Title A. M. 1998, ApJ, 495, 973
Bianda M., Solanki S. K., Stenflo J. O. 1998, A&A, 331, 760
Brandt P. N., Rutten R. J., Shine R. A., Trujillo Bueno J. 1992, in M. S. Giampapa, J. A. Bookbinder (eds.), Cool Stars, Stellar Systems, and the Sun, Proc. Seventh Cambridge Workshop, Astron. Soc. Pac. Conf. Series 26, p. 161
Brandt P. N., Rutten R. J., Shine R. A., Trujillo Bueno J. 1994, in R. J. Rutten, C. J. Schrijver (eds.), Solar Surface Magnetism, NATO ASI Series C 433, Kluwer, Dordrecht, p. 251
Carlsson M., Stein R. F. 1992, ApJ, 397, L59
Carlsson M., Stein R. F. 1994, in M. Carlsson (ed.), Chromospheric Dynamics, Proc. Miniworkshop, Inst. Theor. Astrophys., Oslo, p. 47
Carlsson M., Stein R. F. 1995, ApJ, 440, L29
Carlsson M., Stein R. F. 1997, ApJ, 481, 500
Cheng Q.-Q., Yi Z. 1996, A&A, 313, 971
Cram L. E. 1972, Solar Phys., 22, 375
Cram L. E., Damé L. 1983, ApJ, 272, 355
Damé L. 1985, in H. U. Schmidt (ed.), Theoretical Problems in High Resolution Solar Physics, MPA/LPARL Workshop, Max-Planck-Institut für Physik und Astrophysik MPA 212, München, p. 244
Damé L., Gouttebroze P., Malherbe J.-M. 1984, A&A, 130, 331
Damé L., Martić M. 1987, ApJ, 314, L15
Damé L., Martić M. 1988, in J. Christensen-Dalsgaard, S. Frandsen (eds.), Advances in Helio- and Asteroseismology, IAU Symp. 123, Reidel, Dordrecht, p. 433
Deubner F.-L., Fleck B. 1990, A&A, 228, 506
Elmore D. F., Lites B. W., Tomczyk S., Skumanich A. P., Dunn R. B., Schuenke J. A., Streander K. V., Leach T. W., Clambellan C. W., Hull H. K., Lacey L. B. 1992, Procs. SPIE, 1746, 22
Faurobert-Scholl M. 1993, A&A, 268, 765
Fleck B., Schmitz F. 1991, A&A, 250, 235
Fleck B., Schmitz F. 1993, A&A, 273, 671
Goode P. R., Strous L. H., Rimmele T. R., Stebbins R. T. 1998, ApJ, 495, L27
Hale G. E., Ellerman F. 1904, ApJ, 19, 41
Harvey J. 1977, Highlights of Astronomy, 4 Part II, 223
Hoekzema N. M., Brandt P. N., Rutten R. J. 1998, A&A, 333, 322
Hoekzema N. M., Rutten R. J. 1998, A&A, 329, 725
Hofmann J., Steffens S., Deubner F. L. 1996, A&A, 308, 192
Kalkofen W. 1989, ApJ, 346, L37
Kalkofen W. 1990, in E. R. Priest, V. Krishan (eds.), Basic Plasma Processes on the Sun, IAU Symp., Kluwer, Dordrecht, p. 197
Kalkofen W. 1991, in P. Ulmschneider, E. Priest, B. Rosner (eds.), Mechanisms of Chromospheric and Coronal Heating, Heidelberg Conference, Springer Verlag, Berlin, p. 54
Kalkofen W. 1996, ApJ, 468, L69
Kalkofen W., Rossi P., Bodo G., Massaglia S. 1994, A&A, 284, 976
Kariyappa R., Sivaraman K. R., Anadaram M. N. 1994, Solar Phys., 151, 243
Keller C. U., Deubner F. L., Egger U., Fleck B., Povel H. P. 1994, A&A, 286, 626
Kneer F., Von Uexkull M. 1993, A&A, 274, 584
Kulaczewski J. 1992, A&A, 261, 602

[4] E.g. at URL http://vestige.lmsal.com/TRACE

Landi Degl' Innocenti E. 1998, Nature, 392, 256
Lee J., Chae J.-C., Yun H. S., Zirin H. 1997, Solar Phys., 171, 269
Leibacher J., Gouttebroze P., Stein R. F. 1982, ApJ, 258, 393
Lighthill M. J. 1952, Proc. R. Soc. Lond. A, 211, 564
Lin H. 1995, ApJ, 446, 421
Lites B. W. 1996, Solar Phys., 163, 223
Lites B. W., Elmore D. F., Seagraves P., Skumanich A. P. 1993a, ApJ, 418, 928
Lites B. W., Leka K. D., Skumanich A., Martínez Pillet V., Shimizu T. 1996, ApJ, 460, 1019
Lites B. W., Low B. C., Martínez Pillet V., Seagraves P., Skumanich A., Frank Z. A., Shine R. A., Tsuneta S. 1995, ApJ, 446, 877
Lites B. W., Martínez Pillet V., Skumanich A. 1994, Solar Phys., 155, 1
Lites B. W., Rutten R. J., Kalkofen W. 1993b, ApJ, 414, 345
Lites B. W., Thomas J. H., Bogdan T. J., Cally P. S. 1998, ApJ, 497, 464
Liu S.-Y., Skumanich A. 1974, Solar Phys., 38, 105
Livingston W., Harvey J. 1971, in R. Howard (ed.), Solar Magnetic Fields, IAU Symposium 43, Reidel, Dordrecht, p. 51
Loefdahl M. G., Berger T. E., Shine R. S., Title A. M. 1998, ApJ, 495, 965
Martínez Pillet V., Lites B. W., Skumanich A. 1997, ApJ, 474, 810
Mein P., Mein N., Malherbe J. M., Damé L. 1987, A&A, 177, 283
Meunier N., Solanki S. K., Livingston W. C. 1998, A&A, 331, 771
Musielak Z. E., Rosner R., Stein R. F., Ulmschneider P. 1994, ApJ, 423, 474
Nindos A., Zirin H. 1998, Solar Phys., 179, 253
Noyes R. W. 1967, in R. N. Thomas (ed.), Aerodynamic Phenomena in Stellar Atmospheres, IAU Symp. 28, Academic Press, London, p. 293
Rabin D. 1992, ApJ, 391, 832
Rammacher W., Ulmschneider P. 1992, A&A, 253, 586
Rast M. P. 1995, ApJ, 443, 863
Remling B., Deubner F. L., Steffens S. 1996, A&A, 316, 196
Restaino S. R., Stebbins R. T., Goode P. R. 1993, ApJ, 408, L57
Rimmele T., von der Lühe O., Wiborg P., Widener A. L., Spence G., Dunn R. B. 1991, in M. Ealey (ed.), Active and Adaptive Optical Systems, Proceedings SPIE, Vol. 1542, San Diego, p. 186
Rimmele T. R., Goode P. R., Harold E., Stebbins R. T. 1995, ApJ, 444, L119
Roudier T., Malherbe J. M., November L., Vigneau J., Coupinot G., Lafon M., Muller R. 1997, A&A, 320, 605
Rutten R. J. 1994, in M. Carlsson (ed.), Chromospheric Dynamics, Proc. Miniworkshop, Inst. Theor. Astrophys., Oslo, p. 25
Rutten R. J. 1995, in J. T. Hoeksema, V. Domingo, B. Fleck, B. Battrick (eds.), Helioseismology, Proc. Fourth SOHO Workshop, ESA SP–376 Vol. 1, ESA Publ. Div., ESTEC, Noordwijk, p. 151
Rutten R. J. 1996, in K. G. Strassmeier, J. L. Linsky (eds.), Stellar Surface Structure, Procs. Symp. 176 IAU, Kluwer, Dordrecht, p. 385
Rutten R. J., de Pontieu B., Lites B. W. 1999, in T. Rimmele, K. Balasubramaniam, R. Radick (eds.), High Resolution Solar Physics: Theory, Observations, and Techniques, Procs. 19th NSO/Sacramento Peak Summer Workshop, Astron. Soc. Pac. Conf. Series, in press
Rutten R. J., Uitenbroek H. 1991a, Solar Phys., 134, 15
Rutten R. J., Uitenbroek H. 1991b, in P. Ulmschneider, E. R. Priest, R. Rosner (eds.), Mechanisms of Chromospheric and Coronal Heating, Proc. Heidelberg Conf., Springer Verlag, Berlin, p. 48
Schrijver C. J., Title A. M., Van Ballegooijen A. A., Hagenaar H. J., Shine R. A. 1997, ApJ, 487, 424
Sivaraman K. R. 1991, in P. Ulmschneider, E. Priest, B. Rosner (eds.), Mechanisms of Chromospheric and Coronal Heating, Heidelberg Conference, Springer Verlag, Berlin, p. 44
Sivaraman K. R., Livingston W. C. 1982, Solar Phys., 80, 227
Skumanich A., Lites B. W., Martínez Pillet V., Seagraves P. 1997, ApJS, 110, 357
Solanki S. K., Zufferey D., Lin H., Rueedi I., Kuhn J. R. 1996, A&A, 310, L33
Steffens S., Hofmann J., Deubner F. L. 1996, A&A, 307, 288
Stein R. F. 1967, Solar Phys., 2, 285
Stenflo J. O. 1994, Solar Magnetic Fields, Polarized Radiation Diagnostics, Kluwer, Dordrecht
Sutmann G., Ulmschneider P. 1995a, A&A, 294, 232
Sutmann G., Ulmschneider P. 1995b, A&A, 294, 241
Theurer J., Ulmschneider P., Kalkofen W. 1997, A&A, 324, 717
Von Uexkuell M., Kneer F. 1995, A&A, 294, 252
Wang H., Tang F., Zirin H., Wang J. 1996, Solar Phys., 165, 223
Wang J., Wang H., Tang F., Lee J. W., Zirin H. 1995, Solar Phys., 160, 277
Wellstein S., Kneer F., Von Uexkuell M. 1998, A&A, 335, 323
Zhang J., Lin G., Wang J., Wang H., Zirin H. 1998, Solar Phys., 178, 245
Zirin H. 1995, Solar Phys., 159, 203
Zwaan C. 1987, ARA&A, 25, 83